Analysis procedures accounting for load redistribution mechanisms in masonry earth retaining structures under traffic loading
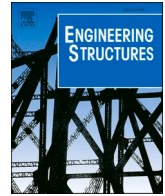
Sharma, Satyadhrik; Longo, Michele; Messali, Francesco

Important note
To cite this publication, please use the final published version (if applicable).
Please check the document version above.

Analysis procedures accounting for load redistribution mechanisms in masonry earth retaining structures under traffic loading

Satyadhrik Sharma [*], Michele Longo, Francesco Messali

Department of Materials, Mechanics, Management & Design, Section of Applied Mechanics, Faculty Of Civil Engineering and Geosciences, Delft University of Technology (TU Delft), Stevinweg 1, 2628 CN Delft, the Netherlands

A B S T R A C T

This paper introduces novel analysis procedures for the structural assessment of masonry earth retaining structures subjected to traffic loading. Given their substantial presence, particularly in transportation networks of historical cities, and the challenges posed by ageing, deterioration, and exposure to loads beyond their original design considerations, this research highlights the necessity of accounting for potential load redistribution mechanisms during their assessment. This can prevent overly conservative interventions that may not be necessary and also contravene sustainability and heritage preservation principles. Four distinct analysis procedures – 2D monotonic, 3D monotonic, 3D static moving load and 3D dynamic moving load – are developed, each progressively more refined than its predecessor in capturing potential load redistribution mechanisms in masonry earth retaining structures. These mechanisms may develop due to the dynamic loading conditions of the vehicular passage, the 3D structural configuration of retaining structures, and non-linear material behaviour. By comparing the structural capacity evaluated using the four procedures, contributions from different sources of load redistribution can be separately quantified, aiding in the reduction of conservatism inherent in less refined assessment procedures. The application of the developed procedures and consequent quantification of load redistribution is demonstrated through a case study of an existing masonry retaining structure in Amsterdam, the Netherlands.

1. Introduction

Masonry earth retaining structures form an integral part of global transportation networks, with a significant presence in several countries worldwide, including (but not limited to) the Netherlands [1,2], the United Kingdom [3–5], France [6], the United States [7] and India [8]. Despite their long service life under challenging environmental conditions, many of these structures are still operational and continue to play a crucial role in maintaining the integrity of transportation networks. Additionally, while they were originally designed to resist primarily static loads, dynamic loading imposed on them by vehicle movements is becoming increasingly relevant due to escalating axle loads of modern vehicles [9]. This situation leaves their stakeholders with an ageing inventory of structures which are not only experiencing accelerated rates of deterioration but are also under greater loading demands.

Design procedures for new retaining structures fall short in assessing existing structures, as they fail to consider various sources of load redistribution. Often, this leads to conservative predictions, meaning

that the actual damage observed in structures is significantly less than the damage estimated by the recommended procedures. This discrepancy between theoretical calculations and real-world observations tends to result in overly cautious assessments. Premature interventions, prompted by conservative yet imprecise predictions, can entail significant economic and environmental costs, underscoring the need for more precise and reliable assessment methods. Such conservatism increases the likelihood of unnecessary repairs and replacements, thereby contravening sustainability principles and deviating from the ethos of minimal intervention – 'as much as needed, as little as possible' – which is crucial for the preservation of heritage structures. Additionally, the structural assessment of these structures frequently depends also on qualitative judgments, primarily based on visual inspections or monitoring of deformations [10,11]. While practical, this approach may not yield accurate estimations of the structural health, unless the deformation limits used to take decisions are grounded in numerical analysis procedures that comprehensively account for potential load redistribution sources in masonry earth retaining structures. Surveys [12] have

* Corresponding author.
E-mail address: S.Sharma-9@tudelft.nl (S. Sharma).

also underscored governmental agencies' concerns over insufficient infrastructure investment, particularly in adapting to increasing demands. This further underscores the imperative of deploying refined analysis procedures for more strategic infrastructure investment.

It is widely recognized that analysis procedures unable to capture the load redistribution mechanisms are inadequate for the assessment of masonry structures [13], due to the limited tensile strength of masonry. Consequently, for the safety assessment of existing masonry structures, the consideration of the gradual evolution of cracking is of paramount importance. Their load-carrying capacity depends largely on the distribution of stresses within the structure itself. Thus, it is crucial that any developed analysis procedures adequately account for all the different sources of load redistribution that can arise. The ability of an analysis procedure to account for load redistribution depends on both how structural configuration (including material behaviour) and loading conditions are modelled [14]. The existing literature offers a multitude of modelling strategies for the structural analysis of masonry structures [15]. While these strategies may vary in terms of method and scale of analysis, the selection of the most appropriate method largely depends on the specific problem at hand [13]. Many of these strategies can be applied for the purposes of this paper. Consequently, the main focus of this section of the paper is to develop analysis procedures which can appropriately simulate the loading conditions arising on earth retaining structures due to vehicular traffic on carriageways constructed on top of their backfill. Such loading primarily consists of pressure that propagates through the backfill onto the retaining structure (Fig. 1).

Traffic loads possess a complex nature and it is hard to establish general technical principles for design standards. This complexity is also reflected in the diverse approaches and load values adopted in regulations from various countries [16–19]. Despite this disparity, all codes assume that loads originating from vehicular traffic on retaining structures take the form of a time-invariant overload. The transient nature of loading conditions to which retaining structures are subjected, resulting from the movement of vehicles, is not taken into account. Consequently, the load redistribution behaviour that these retaining structures may exhibit due to variations in loading occurring in both time and space cannot be evaluated using such approaches. Moreover, the use of 3D computational models can be time-consuming and, therefore, still uncommon in engineering practice, where 2D numerical models are used. Such 2D numerical models cannot capture load redistribution along the length of the structures. Additionally, the non-linear behaviour of masonry is often neglected in engineering practice: the models adopt linear-elastic material constitutive laws, preventing any possibility to identify load redistribution effects in the structure.

This paper aims to address the shortcomings described above by introducing analysis procedures specifically designed for masonry earth retaining structures under traffic loading. It is important to note that research in this domain has been relatively scarce. Most existing studies have concentrated on developing analysis procedures for masonry buildings, particularly under extreme conditions like earthquakes [20–22] and explosive loading [23–26] rather than for transportation infrastructure facing less extreme actions such as vehicular traffic. In the cases where masonry infrastructure has been assessed, the emphasis has predominantly been on masonry arch bridges under extreme [27–30] and traffic loading [31–34]. Finally, the analysis of large infrastructure network systems has urgently driven the development of quick and expeditious assessment methods, whose predictions are based on on-field data acquired through various monitoring systems [35,36]. It is important to note that even these methods benefit from and partly rely on the outcomes of detailed predictions obtained from high-fidelity simulations. The proposed paper seeks to contribute to this under-explored area of research by developing comprehensive approaches for evaluating the behaviour of masonry earth retaining structures under traffic loading in Section 2. The developed procedures are then applied in Section 3 to a historic masonry earth retaining wall in Amsterdam, the Netherlands, with an in-depth interpretation of the results obtained. Finally, Section 4 presents the concluding remarks of the paper.

2. Analysis procedures for masonry earth retaining walls under traffic-loading

To address the shortcomings highlighted in Section 1, analysis procedures tailor-made for the structural assessment of masonry earth retaining structures under traffic loading are developed in this paper. The authors have already proposed an analysis procedure for conducting a 3D non-linear dynamic structural assessment of masonry earth retaining structures under traffic loading in [2]. This analysis procedure has the potential to independently account for load redistribution mechanisms arising from the following three sources: 1) dynamic loading conditions arising from the vehicular passage; 2) 3D structural configuration of retaining structures; and 3) non-linear material behaviour. Although advances in numerical simulation tools make the implementation of such analysis procedures more accessible, it is
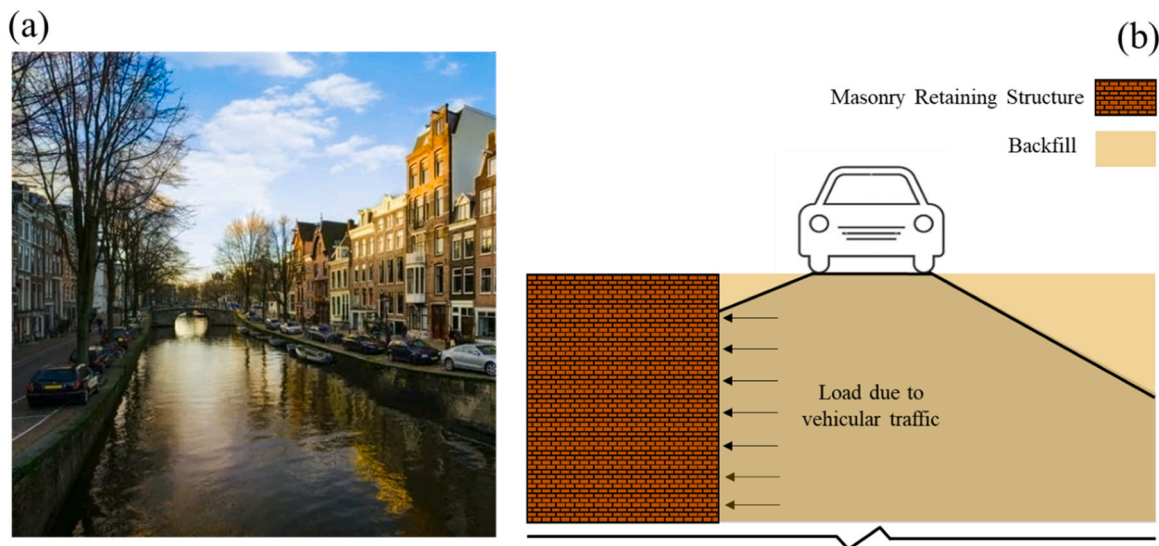

Fig. 1. (a) Vehicular traffic on carriageways constructed on the backfill of masonry retaining walls in Amsterdam, the Netherlands, and (b) schematic showing how this vehicular traffic creates pressure distributed by the soil on the masonry retaining structure.

expected that 2D linear-elastic analysis will remain the standard assessment procedure in practice. Consequently, complementary analysis procedures are proposed in this paper to separately quantify the contribution to load redistribution of each of these sources, and consequently to reduce the degree of conservatism that is implicit in less refined assessment procedures. Each procedure is less refined than the one described in [2] in one of the aforementioned three aspects. The considered analysis procedures, including the 3D non-linear dynamic procedure, can be broadly categorised as moving load (Section 2.1) and stationary monotonic load (Section 2.2) procedures, which are explained in more detail in the following sections.

It should be noted that in all the developed analysis procedures, a two-tier sub-structured modelling approach is adopted, similar to the methods used for earth retaining structures in [37] and buildings in [38–43]. In this approach, the system consisting of the masonry retaining structure and the adjacent soil is divided into two separate subsystems. The first subsystem, considered in Tier 1, includes the soil and the pavement impacted by vehicular traffic. The second subsystem, modelled in Tier 2, comprises solely the masonry earth retaining structure. This sub-structured approach is adopted for the 3D non-linear dynamic analysis procedure in [2] to facilitate simulating vehicles passing over numerical models of lengthy retaining structures, while avoiding the prohibitively heavy computational burden of explicitly modelling a 3D soil block in such scenarios. The two-tier approach is consistently adopted in all complementary procedures developed in this paper to facilitate an unbiased quantification of the various load redistribution mechanisms mentioned above.

2.1. Moving load procedures

Moving load procedures are designed to simulate the movement of a vehicle or vehicular traffic along the length of the retaining structure. This movement exerts pressures on the retaining structures, as illustrated in Fig. 1. If the vehicle's speed is considered while applying the pressures, a dynamic moving load procedure is used. Alternatively, if the

speed is disregarded, a static moving load procedure can be adopted. By comparing the structural capacity evaluated using these complementary procedures, i.e. dynamic vs. static moving load, on the same 3D numerical model, it is possible to quantify the load redistribution that arises solely from the consideration of dynamic vs. static loading conditions.

2.1.1. 3D dynamic moving load procedure

The 3D dynamic moving load procedure has been previously introduced by the authors in [2]. For ease of understanding and to facilitate the discussion made in the following sections, the key features of this procedure are summarised here. As mentioned earlier, a two-tier modelling approach is adopted for all analysis procedures in this paper. In Tier 1, the focus is on the first sub-system, which is analysed with a 3D solid numerical model, comprising of the soil and road pavement. The pavement is important because of its ability to distribute vehicular loads [44]. All elements of this model are assigned linear-elastic properties. The modelled soil block is selected to be sufficiently large to capture the entire pressure distribution on the retaining structure resulting from vehicular movement. To simulate the effect of an infinite medium and prevent wave reflection, absorbing boundary conditions are applied at the external faces of the soil block [45].

On the Tier 1 model, a dynamic analysis is carried out to simulate the passage of a vehicle over a limited distance (Δd). This is achieved by impulsively applying the vehicle's weight at each wheel's contact point with the pavement. This effectively simulates the vehicle's movement over Δd, as depicted in Fig. 2a. As the wheel approaches the point of contact, vertical stresses increase, peaking when the wheel is directly above it, and then diminishing as the wheel moves away. Each wheel load is modelled individually, allowing in principle the description of any vehicular load – defined by axle loads and spacing configurations – to be considered in Tier 1. In this simulation, the distribution of normal compressive stresses at the retaining structure's location is continuously recorded under the applied vehicular load. A specific point is selected when the stress distributions on the two surfaces yield the maximum net
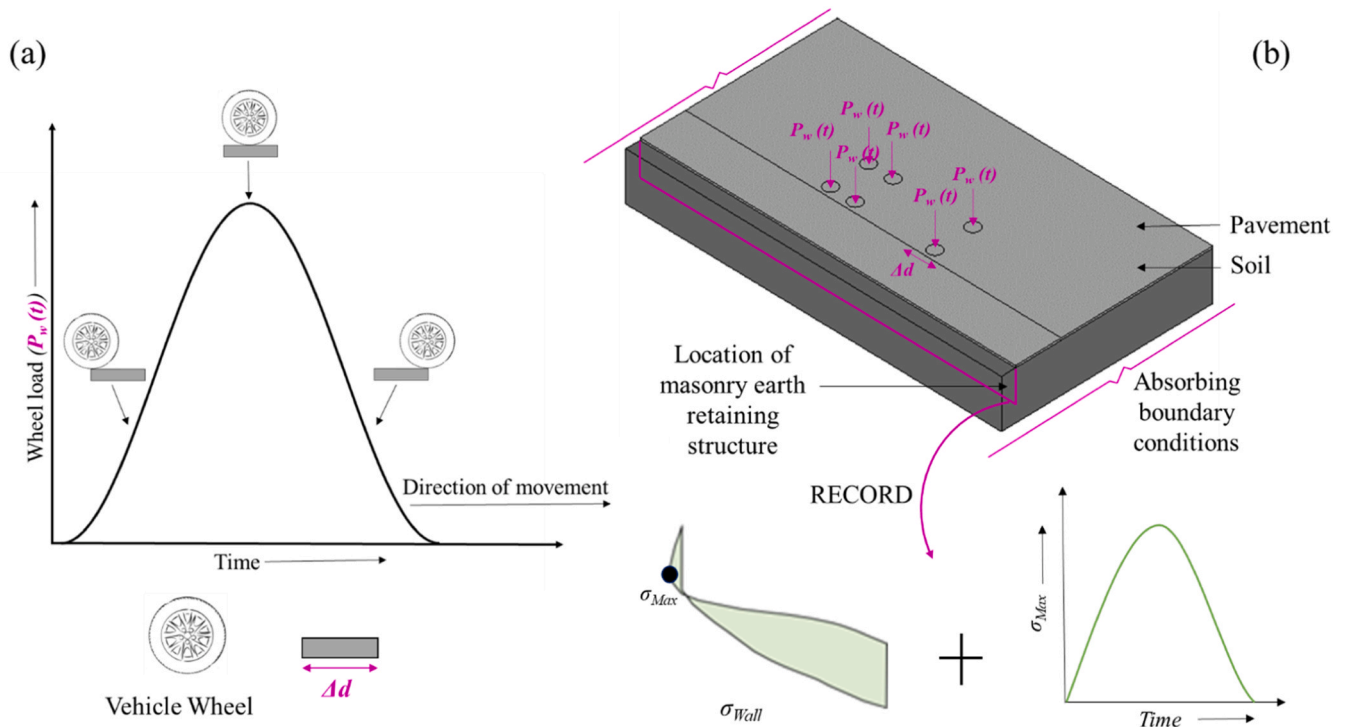

Fig. 2. Schematic illustrating: (a) the simulation of a wheel's passage over a limited distance by impulsively applying its load, and (b) the numerical model used and the recordings obtained from it in Tier 1 (Note: σ_{Wall} represents the distribution of normal compressive stresses on the retaining wall resulting from vehicular traffic on its backfill).

compressive force. The stress distributions at this instant determine the load (σ_{Wall}) to be applied in Tier 2. Additionally, the time-history (σ_{Max} vs. time) of the maximum stresses (σ_{Max}) in σ_{Wall} is recorded for use in Tier 2 (Fig. 2b).

In Tier 2, the focus shifts to the second sub-system, comprising the earth retaining structure that is being assessed. A dynamic analysis is carried out on a non-linear 3D numerical model to account for load redistribution mechanisms. Although the soil block is not included in this model, its impedance is represented through the use of springs or boundary interface elements. Either the entire length of the retaining structure can be modelled in Tier 2, or a reduced length can be adopted based on the findings of a parametric study. This study would investigate the impact of the model's length on the displacements exhibited or the failure mechanism under vehicular loads.

The dynamic movement of the vehicle, considered in Tier 1, is simulated along the retaining structure by applying the recorded stress distribution σ_{Wall}. This is done as a series of normal pressure loads, combined with the time-histories of their maxima, σ_{Max} (Fig. 2). These pressure loads are applied to a sequence of consecutive sections along the wall, each section being shifted by Δd – the same limited distance over which the vehicle's passage was simulated in Tier 1. A time difference of Δt, the time required for the vehicle to traverse Δd at the considered speed, is maintained between load applications on subsequent sections. This approach ensures considering both the time-history of the maximum stresses and the distributions generating the largest compressive forces on the retaining structure, making the procedure both simplified and conservative. A schematic detailing this procedure as the vehicle moves across $2 \times \Delta d$ sections from Fig. 3a to Fig. 3d is provided.

2.1.2. 3D static moving load procedure

This complementary analysis procedure is performed to separately quantify the load redistribution contribution arising from the dynamic vs. static application of traffic loads. To isolate this contribution, the applied traffic load in this procedure must also simulate the passage of a vehicle along the length of the retaining structure, similar to the 3D dynamic moving load procedure. However, for traffic loads to be applied statically, the vehicle must be assumed to be travelling along the length of the structure at an infinitely slow rate i.e. under a static hypothesis. This requires modifications to both tiers of the two-tiered sub-structured approach. In Tier 1, the weight of the vehicle is no longer applied impulsively, rather statically. Consequently, the stress distribution on the retaining structure needs to be recorded when the complete weight of the vehicle has been applied. In Tier 2, the zero speed of the vehicle causes Δt to become infinitely long. Consequently, the retaining structure is subjected to a single σ_{Wall} stress distribution at any given instant as the vehicle travels along it. To achieve this result, the σ_{Wall} distribution associated with the subsequent Δd segment is applied only after the retaining structure has been completely unloaded from the stress distributions associated with the preceding Δd segment. The schematic provided in Fig. 4 details this procedure through four different stages of a 3D static moving load analysis, highlighting its difference from the analogous procedure adopted for the 3D dynamic moving load procedure depicted in Fig. 3. As the analysis procedure is static, there is no effect of the rate at which the retaining structure is loaded or unloaded, i.e. the shape of σ_{Max} vs. load step in Fig. 4 (which controls the amplitude of σ_{Wall} at any load step in the analysis) does not have any effect on the results of the procedure.

Both dynamic and static moving load procedures are readily applicable for serviceability limit state verifications. However, to evaluate the load-carrying capacity of the retaining structure at the ultimate limit state, a single vehicle passage may not suffice. For such evaluations, incremental analyses similar to Incremental Dynamic Analysis [46], which is commonly used for structures under seismic loading, can be
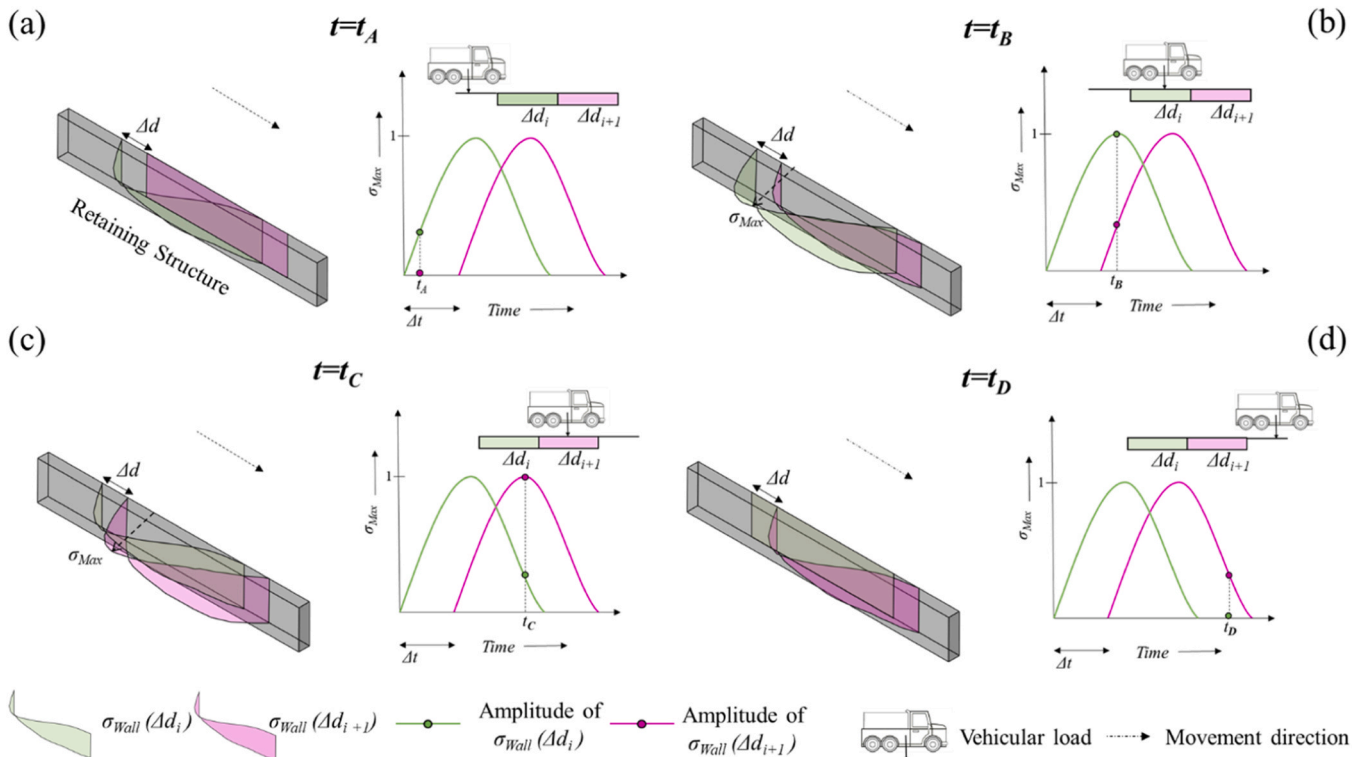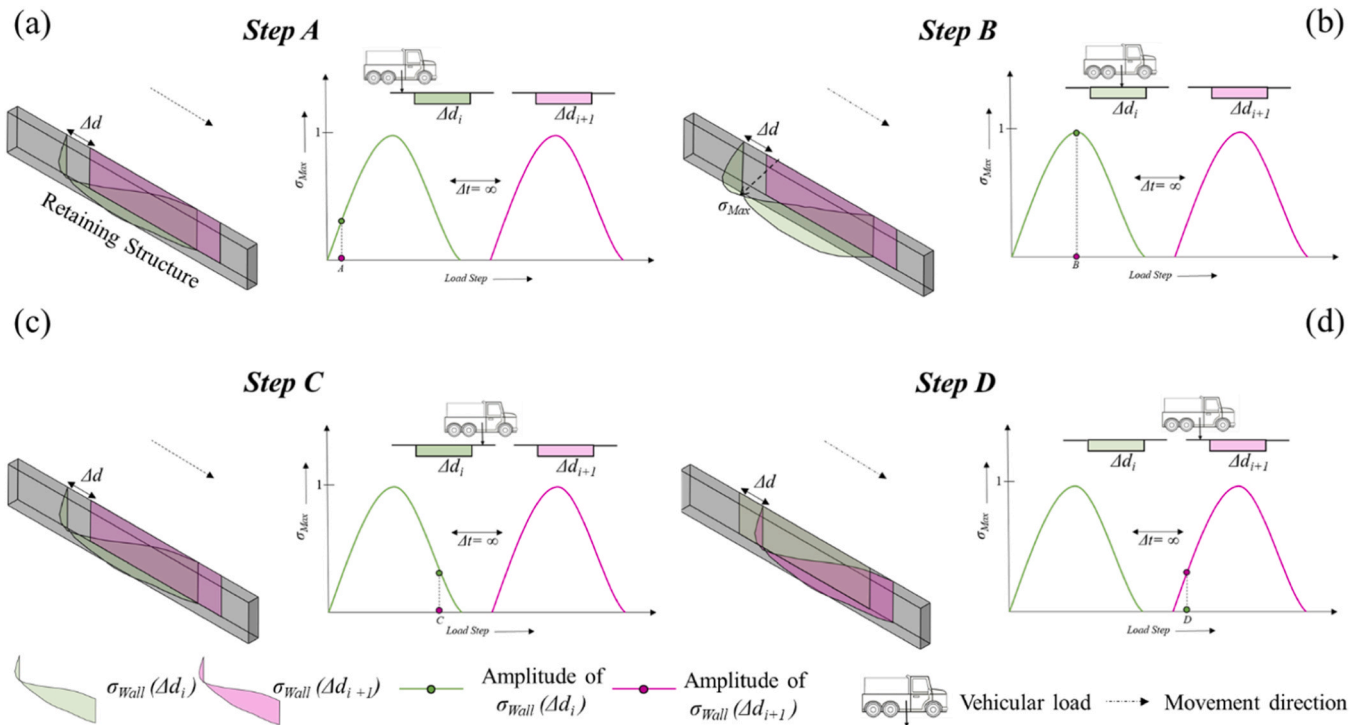

Fig. 3. Schematic illustration of how recordings from Tier 1 are applied in Tier 2 to the retaining structure in the 3D dynamic moving load procedure: (a) the vehicle is approaching segment Δd_i; (b) the vehicle is in the middle of segment Δd_i and approaching segment Δd_{i+1}; (c) the vehicle is receding from segment Δd_i and is in the middle of segment Δd_{i+1} and (d) the vehicle is receding from segment Δd_{i+1} (Note: σ_{Wall} represents the distribution of normal compressive stresses on the retaining wall resulting from vehicular traffic on its backfill).
Adapted from [2].

Fig. 4. Schematic illustration of how recordings from Tier 1 are applied in Tier 2 to the retaining structure in the 3D static moving load procedure (a) the vehicle is approaching segment Δd_i; (b) the vehicle is in the middle of segment Δd_i; (c) the vehicle is receding from segment Δd_i and (d) the vehicle is approaching segment Δd_{i+1} (Note: σ_{Wall} represents the distribution of normal compressive stresses on the retaining wall resulting from vehicular traffic on its backfill).

implemented. These analyses progressively increase the load associated with the vehicle's passage to assess the structural capacity of the retaining structure. Within the proposed methodology, this escalation entails scaling up the σ_{Wall} recordings from the Tier 1 model, which is performed on a linear elastic numerical model, by multiplying them with a scalar *Load Multiplier (LM)*. In each analysis corresponding to a specific *LM*, the wall is initially considered undamaged, then subjected to the passage of a vehicle with a weight scaled up by the factor of the Load Multiplier. A demonstration of incremental analyses using the moving load procedures is provided in Section 3.2.2.

2.2. Stationary monotonic load procedures

The second category of analysis procedures for the assessment of earth retaining structures under traffic loading are stationary monotonic load procedures. Unlike moving load procedures, these analysis procedures do not simulate the movement of the vehicle. The vehicle is instead assumed to be stationary and its weight is gradually and monotonically increased to evaluate the structural capacity of the retaining structure. Depending on whether the assessment is carried out in Tier 2 on a 3D numerical model or a 2D numerical model, either 3D or 2D monotonic procedures are proposed. Non-linear models are adopted in both cases for Tier 2. By comparing the structural capacities evaluated using these complementary procedures, it is possible to quantify the load redistribution that arises solely from the consideration of a 3D structural configuration of retaining structures. As both procedures are also static, the same Tier 1 analysis used for the 3D static moving load procedure can be used, i.e. the weight of the vehicle is applied statically to the Tier 1 model and the stress distribution on the retaining structure is recorded when the complete weight of the vehicle has been applied.

2.2.1. 3D monotonic load procedure

For the 3D monotonic load procedure, the analyses are performed using a 3D numerical model in Tier 2. As the movement of the vehicle is not considered, a single σ_{Wall} recordings obtained from the Tier 1

analysis can be directly applied to this model. To evaluate the structure's load-carrying capacity at the ultimate state, this σ_{Wall} recording is monotonically increased by multiplying it with a scalar *Load Multiplier (LM)* (Fig. 5a). It should be noted that despite using the same Tier 1 analysis and even the same 3D numerical model in Tier 2, the load-carrying capacities evaluated using the 3D monotonic load and the 3D moving load procedures, adopting an incremental analysis procedure, cannot be directly compared. This is because they simulate different physical scenarios, i.e. the 3D monotonic load procedure does not consider the movement of the vehicle.

2.2.2. 2D monotonic load procedure

For the 2D monotonic load procedure, each analysis is performed using a 2D numerical model in Tier 2. This approach is currently the standard assessment tools adopted in engineering practice, which is expected not to change in the near future. Typically, the model is assigned a limited depth, usually of unit length (i.e. 1 m) or, for masonry earth retaining structures supported on pile foundations, to the longitudinal axial spacing between rows of piles, as it will be assumed in Section 3.

Consequently, unlike in the 3D monotonic load procedure, the σ_{Wall} recordings from the Tier 1 analysis cannot be directly applied to the 2D model, as these recordings correspond to stresses distributed over a length ΔL, much longer than the depth of the sectional models. Additionally, by their very nature 2D sectional models apply stresses varying only over the height of the retaining structure. To avoid bias from the 3D structure's configuration, multiple 2D analyses are required, differing only in the σ_{Wall} distribution vs. the height, extracted from the Tier 1 analysis at various locations along ΔL (Fig. 5b). Theoretically, a very large number of 2D monotonic analyses can be conducted by picking up the 2D σ_{Wall} vs. height distributions (for example, $\sigma_{2D\ i}$ and $\sigma_{2D\ i+n}$ in Fig. 5b) at any point along 3D σ_{Wall}. In practice, guided by sound engineering judgement, this number can be pragmatically limited to a reasonable number of σ_{Wall} vs. height distributions. Furthermore, by comparing the structural capacities from both the 3D and 2D monotonic
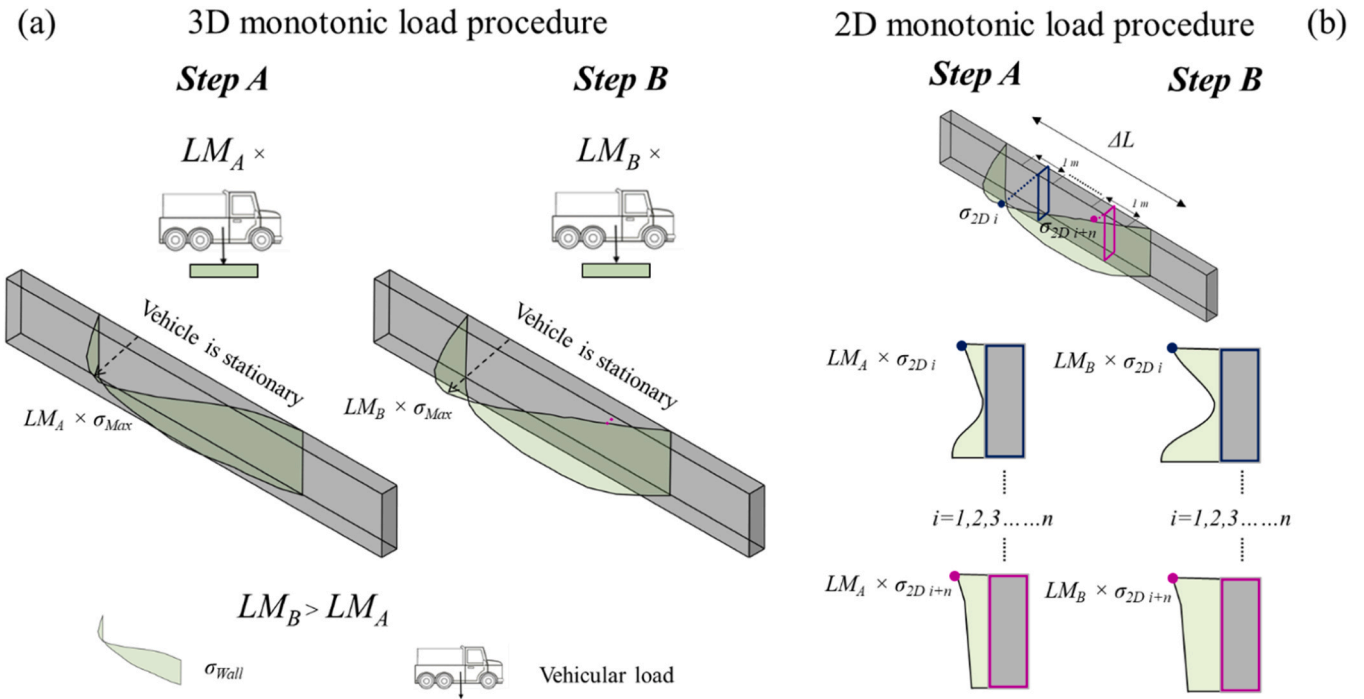
Fig. 5. Schematic explaining how recordings of tier 1 are applied in tier 2 to the retaining structure in the (a) 3D and (b) 2D monotonic load procedures (Note: σ_{Wall} represents the distribution of normal compressive stresses on the retaining wall resulting from vehicular traffic on its backfill).

load procedures, quantification of load redistribution due to the 3D nature of retaining structures can be calculated. However, since multiple 2D analyses are performed, this quantification does not result in a single value but rather in a range, determined by the analyses yielding the lowest and highest structural capacities in the 2D monotonic load procedure.

2.3. Analytical alternatives to Tier 1 for predicting stress distribution on earth-retaining structures

With the exception of the 3D dynamic moving load procedure, Tier 1 can be replaced by analytical formulations to enhance computational efficiency. However, it should be noted that such formulations cannot account for boundary non-linearities that can be easily considered in the numerical simulations of Tier 1. Several works, including but not limited to [44,47–49], discuss closed-form analytical formulations for estimating stresses within a soil body. Notably, these works build upon the contributions of Boussinesq [50], who analyzed the stress distribution within an elastic isotropic infinite half-space under a point load. Similar to the numerical models utilized for Tier 1, the wheels of vehicles can be idealized as concentrated loads acting at their point of contact with the pavement. The horizontal normal stress $q_x(y,z)$, computed at any point on the retaining structure and at a distance x from the point load Q (Fig. 6) can be calculated as per Eq. 1a as per Frazee [49], where ν
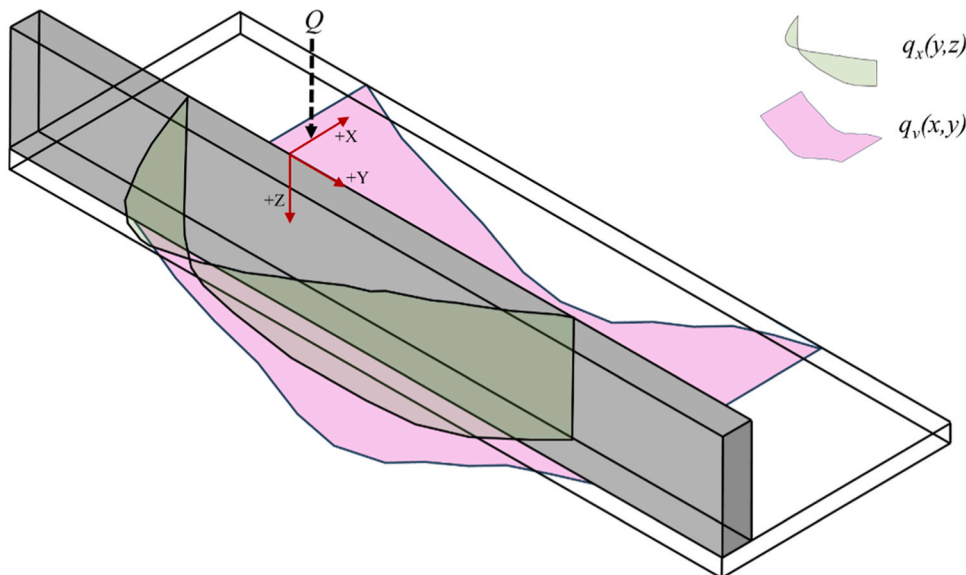

Fig. 6. Coordinate system adopted for the formulae provided in Eq. 1a and Eq. 1b for calculating horizontal and vertical stresses acting normally to the earth retaining structure due to the concentrated load Q (schematic for illustrative purposes).

represents the Poisson's ratio of the soil. If horizontal structural components, such as timber floors, are present in the retaining structure, vertical normal stresses arising due to vehicular traffic are also computed. The vertical stress q_v *(x,y)* on horizontal components of the retaining structure, computed at a distance z from the point load Q, can be calculated as per Eq. 1b:

$$q_x(y,z) = \frac{\psi Q}{2\pi}\left[\frac{3x^2z}{(x^2+y^2+z^2)^{\frac{5}{2}}} - \frac{1-2\nu}{(x^2+y^2+z^2)+z\sqrt{x^2+y^2+z^2}}\right]$$

(1a)

$$q_v(x,y) = \frac{3Q}{2\pi}\frac{z^3}{R^5} = \frac{3Qz^3}{2\pi}(x^2+y^2+z^2)^{-\frac{5}{2}}$$

(1b)

The stress distributions computed via these formulations are compared to their counterparts evaluated through finite element simulations in Section 3 for the 3D monotonic load procedure, where the developed analysis procedures are applied to a case study.

3. Application of the developed procedures: masonry earth retaining structure

The analysis procedures developed in the preceding sections have been applied to a masonry earth retaining structure, namely a quay wall, in Amsterdam, the Netherlands. Quay walls, engineered to stabilize shorelines, accommodate ships, and protect against water ingress, are a defining feature of the Netherlands' landscape. They are crucial elements of the road transportation networks of numerous historic cities, lining the intricate network of canals that are a part of the unique urban fabric and water management system of the country. Additionally, in a country where a significant portion of the land lies below sea level and faces the risk of riverine flooding [51], quay walls play a vital role in preventing urban inundation. These structures have endured varying degrees of damage throughout their life due to foundation failure, material aging and deterioration, lack of adequate maintenance, and, notably, overloading. Originally designed as gravity retaining walls, the quays are now continuously exposed to dynamic vehicular loads – both different in nature and more significant in magnitude than the loads they were initially designed to withstand. Consequently, the structural

capacity of hundreds of kilometres of quay walls is a subject of concern, as evidenced by several instances of severe damage [52] and even collapse [53].

The procedures are specifically applied to the *Marnixkade* quay in Amsterdam, the same case study adopted in the authors' previous work [2]. This quay features a masonry gravity retaining wall supported by a timber floor and timber piles, interspersed with timber beams (*kespen*) placed between the floor and the foundation piles. Both the wall and the floor are subjected to loading originated by vehicular traffic loads and propagated through the soil. The clay brick masonry wall is on average 0.65 m thick and 1.40 m high. A capstone is placed on top of the wall. Inspections [54] have revealed that the quay, particularly its substructure, has suffered damage over time from environmental factors, diminishing the timber components' dimensions. According to the original plans and the dimensions used in this work, the timber floor is 0.07 m thick, and the beams (*kespen*) have a 0.20 × 0.20 m cross-section and are 2.4 m long, resting on tapered piles. These piles, with diameters ranging from 0.20 to 0.26 m at their caps, are organized in three rows per beam (*kesp*). The longitudinal spacing varies between 0.90 and 1.20 m, with a consistent transverse spacing of 1.10 m. Each pile tapers at approximately 9.75 mm/m along its length. The ground level at *Marnixkade* is 0.58 m above *Normaal Amsterdams Peil* (NAP), and the water level is at − 0.40 m NAP (Fig. 7). NAP denotes the reference plane for water height in the Netherlands, with 0 m NAP approximating the North Sea's average sea level [55]. Cone penetration tests [54] revealed poor soil conditions, which improve only at the first sand layer, reached by the pile tips at approximately − 13 m NAP, resulting in each pile's length being around 12 m.

3.1. Tier 1 analyses

The Tier 1 numerical model developed to assess the *Marnixkade* quay measures approximately 70 m x 28 m x 18 m (*l* x *w* x *h*). It should be noted that the canal bed geometry on the waterside is reproduced in this model. These dimensions were chosen to ensure that the model is sufficiently large to capture the entire pressure distribution on the retaining structure generated by the vehicle during both dynamic and static calculations (Fig. 8a). The vehicle selected for demonstrating the analysis procedures is a 3-axle, 6-wheeled fire truck used in Amsterdam, the Netherlands. This fire truck is considered to be travelling at a distance of
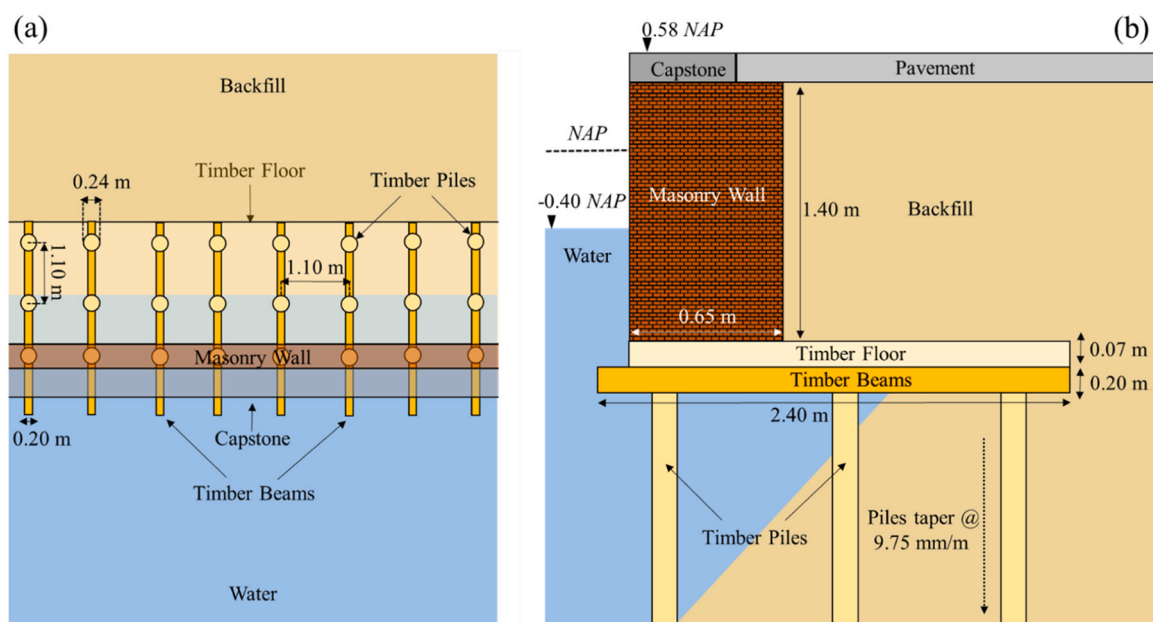

Fig. 7. Geometry of the case-study masonry earth retaining structure, *Marnixkade* in Amsterdam, the Netherlands: (a) plan view and (b) transversal cross-section. Adapted from [2], based on data in [54].
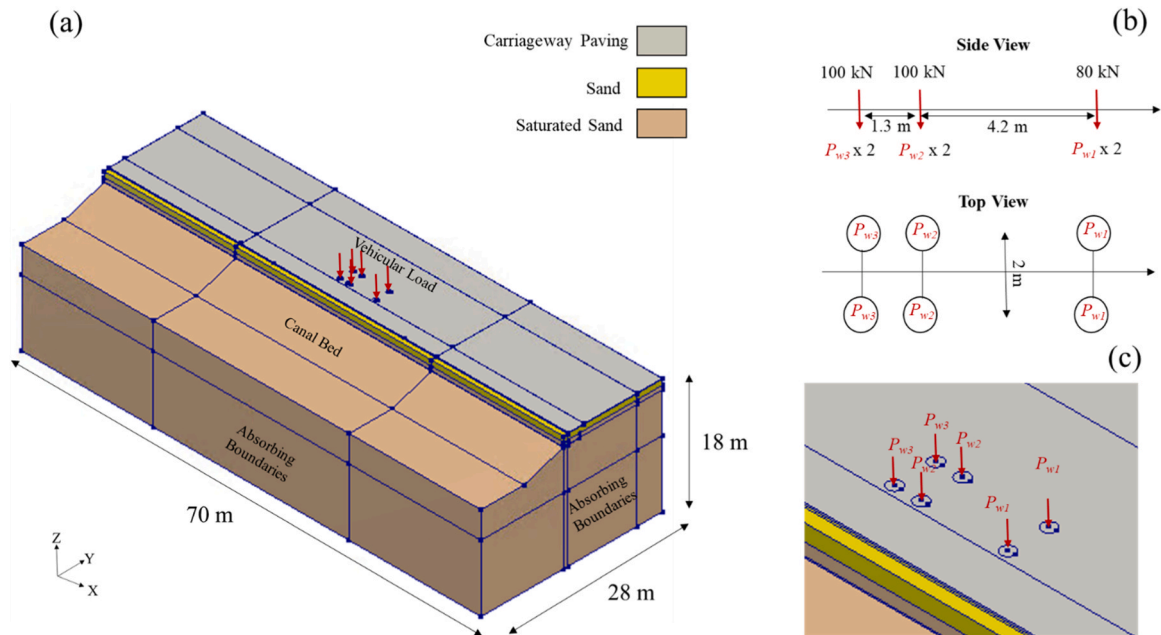
Fig. 8. (a) Numerical model adopted for Tier 1 to demonstrate the developed analysis procedures, (b) axle and wheel load configuration of the fire truck considered as the vehicular load, and (c) close-up of how this vehicular load is applied to the Tier 1 numerical model.

4 m from the quay wall, measured from the inner edge of the masonry quay to the longitudinal central axis of the vehicle. Absorbing boundary conditions [45] are implemented on the external faces of the soil block to simulate the effects of an infinite medium and prevent the reflection of outward waves in the dynamic calculations, except on the waterfront where the wall meets the water. The model also includes a stiffer layer representing the carriageway's paving over which the vehicle travels. Linear-elastic properties are assigned to all model elements. These properties correspond to the compacted sand typically used in Amsterdam for the backfill of quays, with values of 1800 kg/m^3 for material density, 50 MPa for Young's modulus, and 0.35 for Poisson's ratio. Saturated sand is assigned a higher material density of 2000 kg/m^3. For the pavement, values of 2000 kg/m^3 for material density, 2000 MPa for Young's modulus, and 0.25 for Poisson's ratio are used.

For Tier 1 of the 3D dynamic moving load procedure, the movement of the fire truck over a limited distance Δd is simulated by impulsively applying the vehicle's weight through each of its six wheels simultaneously (Section 2.1.1). This demonstration adopts a haversine impulse, shaped to align with the experimental readings reported by Loulizi *et al.* [56], which were obtained from an instrumented pavement during a loaded moving truck's traversal over a pressure cell with a speed of 30 km/h, which is also the speed limit in *Marnixkade*. Consequently, the selected value Δd is consistent with the diameter of the circular pressure cells used in Loulizi *et al.*'s study. As described in Section 2.1.1, the Tier 1 simulation records the normal compressive stress generated by vehicular traffic on surfaces at the positions of both the wall and the floor. σ_{Wall} (and correspondingly, σ_{Floor}) is recorded at the moment when the net compressive force (F_N), derived by integrating the stress distributions on these surfaces, reaches its peak in the dynamic simulation. This net force is computed by summing the stress values across the entirety of the structure's surface area, with each stress value representing the force per unit area. This summation, multiplied by the differential area element, yields the total force exerted on the structure. In this demonstration, the net compressive forces on the wall and the floor peak occur concurrently. The time-history of the maximum stresses in σ_{Wall} (and σ_{Floor}) is also documented. The procedure for Tier 1 of the static analysis procedures, is considerably more straightforward. Here, the vehicle's weight is applied statically through each wheel. σ_{Wall} and σ_{Floor} is recorded once the vehicle's weight is fully applied. The analytical

formulation presented in Section 2.3 is also employed to compute σ_{Wall} and σ_{Floor} for the static analysis procedures. For a 3-axle 6-wheeled fire truck, σ_{Wall} is calculated using this formulation through the linear superposition of the stress distribution caused by each of the 6 wheels, as per Eq. 1a and Eq. 1b. The net compressive forces (F_N) and the max compressive stress corresponding to these different evaluations of σ_{Wall}, i.e., numerical dynamic, numerical static, and analytical static, are also reported in Fig. 9.

Fig. 9 clearly demonstrates that the σ_{Wall} distribution shape is consistent across all three evaluations. In every instance, the maximum compressive stress (σ_{Max}) is observed at the base of the wall, centrally along its length. At the base of the wall, σ_{Wall} reaches its maximum, with both the magnitude and the extent of the stress distribution decreasing towards the top. At the upper sections, the wall experiences tensile stresses due to the of the linear-elastic behaviour of the Tier 1 model, which are unlikely to be transferred through the soil to the retaining structure. Therefore, all tensile stresses identified within the σ_{Wall} distributions are excluded from the Tier 2 analysis. The wall experiences the highest net compressive force (F_N) in the numerical dynamic simulation (Fig. 9a). In the comparison between numerical static (Fig. 9b) and analytical static (Fig. 9c) Tier 1 calculations, the numerical approach yields higher net compressive stresses. This difference presumably stems from how boundaries are treated in the two evaluations. Specifically, in the analytical Tier 1 calculation, the soil is considered an infinite medium, implying the presence of soil on the water-facing side of the quay, which remains free/unrestrained in the numerical model used for Tier 1 calculations (Fig. 8). Each of these σ_{Wall} distributions are used to simulate the effect of traffic loads in the Tier 2 numerical model of *Marnixkade* described in the following section.

3.2. Tier 2 analyses

3.2.1. Numerical models

The Tier 2 numerical model developed to assess the *Marnixkade* quay has the same sectional dimensions as those depicted in Fig. 7. Though the quay is almost 350 m long, only 30 m (L in Fig. 10a) of the quay is modelled in this numerical model. This length is larger than ΔL and is based on a sensitivity study which analysed the effect of the length of the numerical model on the displacements of the quay. In-plane restraints
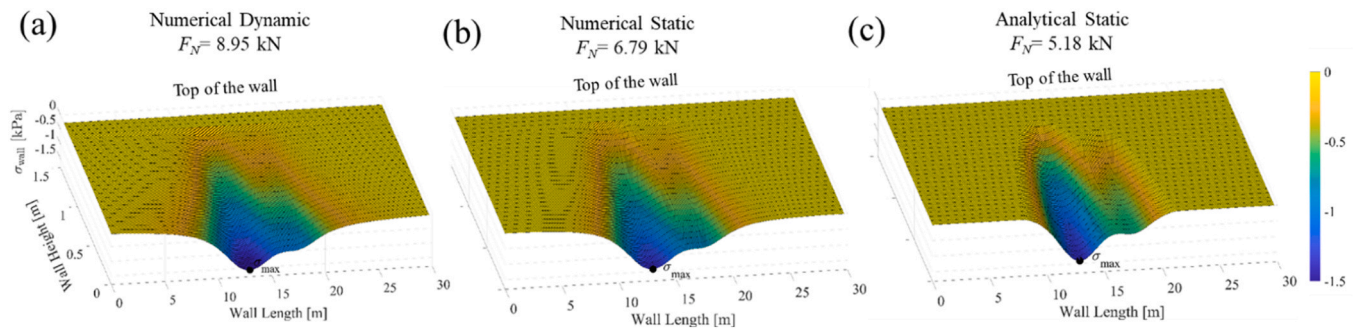
Fig. 9. σ_{Wall} distributions from (a) numerical dynamic, (b) numerical static and (c) analytical static Tier 1 evaluations.
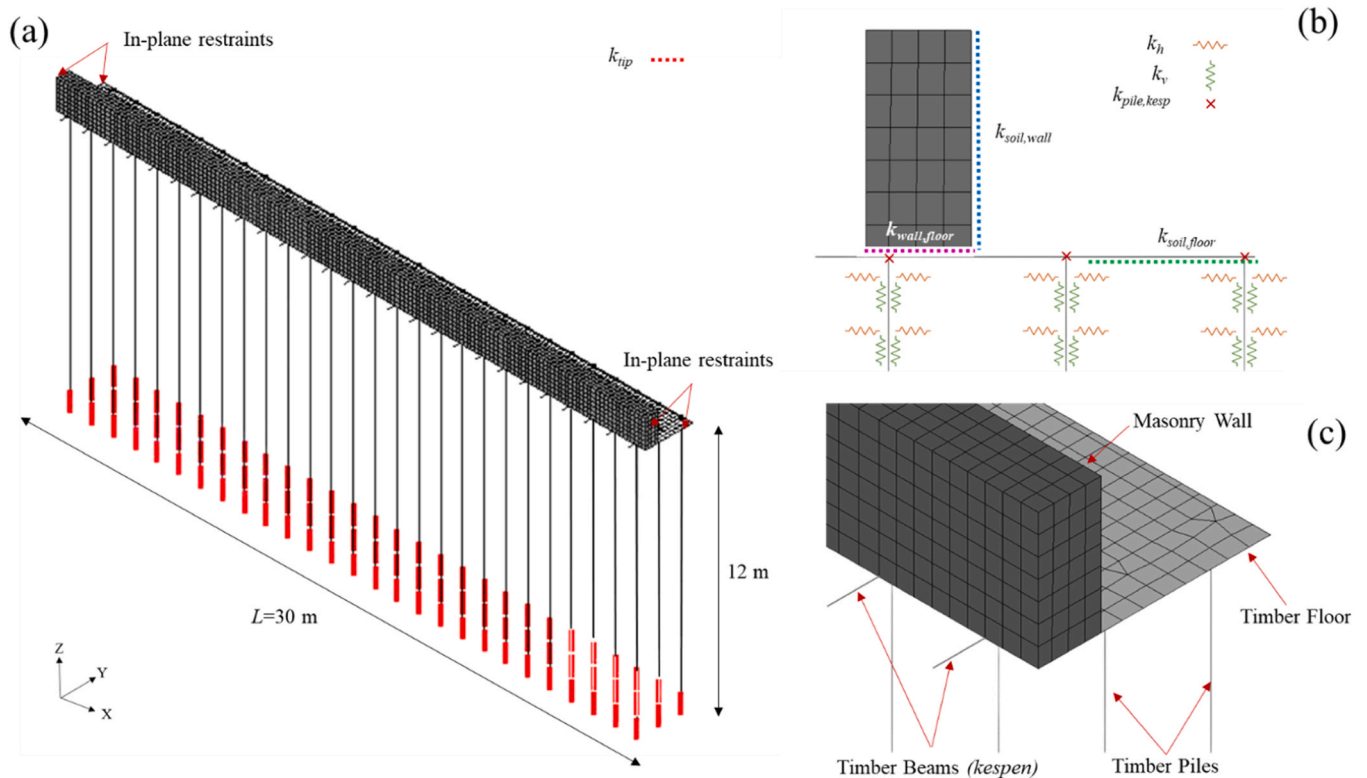

Fig. 10. Numerical model adopted for Tier 2 in the developed analysis procedures: (a) general isometric view; (b) transversal cross-section highlighting different interface elements; (c) close-up of the general isometric view.
Reproduced from [2].

are applied as boundary conditions to simulate the confinement provided by the adjacent portions of the quay not considered in this model (Fig. 10a).

Fig. 7 shows that *Marnixkade* combines masonry and timber constructions. The masonry is simulated with twenty-node isoparametric quadratic solid elements, employing an isotropic material model for both non-linear tensile and compressive behaviors in principal directions, known as the Total Strain Rotating Crack model (TSRCM, [57]). Despite masonry's orthotropic nature, the TSRCM is selected over other isotropic and orthotropic material models [58] due to uncertainty regarding the bond pattern within the wall's 0.65 m thickness. The cracking behavior is quantified for this material model by fracture energy, a parameter represented by the area under the stress-strain curve, with tensile stresses reducing linearly and compression initially hardening and then softening along a parabolic curve. Timber components are modeled as linear-elastic, with failure assessed indirectly in post-processing by comparing developed stresses against predefined material strengths for various failure modes. The timber floor is

represented by eight-node quadratic curved shell elements, and *kespen* and piles by three-node class III beam elements. Pile tapering is represented by segmenting the beam elements into five parts, each with progressively reduced diameters. For the 2D monotonic procedure, 2D plane stress conditions are assumed. A thickness of 1.1 m, corresponding to the longitudinal distance between adjacent piles, is selected for the cross-section of the wall and timber floor. These components are modelled using 8-node quadratic plane stress elements. Unlike the wall and floor, the *kesp* retains its precise cross-sectional dimensions (i.e., it is not assigned a thickness of 1.1 m) and is modelled with beam elements. Similarly, the three wooden piles within the considered 1.1 m section are represented using beam elements, factoring in the spacing between adjacent piles. Composed line elements [57] are used to record the reaction forces in the masonry wall under traffic loading for both 3D and 2D numerical models. These elements store reaction forces by integrating internal forces within the model's elements across their assigned volumes. In the 2D model, a single composed element records the reaction forces across a 1.1 m thick modelled masonry wall. For the 3D

numerical model, reaction forces are recorded along the wall's entire length and for individual 1.1 m sections, aiding in the comparison of structural capacities assessed using 3D and 2D monotonic load methods, as detailed in Section 3.2.3.

The interaction among the quay's structural elements is also modelled. A non-linear interface element represents the mortar joint between the masonry wall and the timber floor, allowing for the simulation of flexural opening and shear sliding ($k_{wall,floor}$ in Fig. 10b). This element's stiffness follows Lourenço's [59] guidelines. The timber floor's connection to the *kespen* is considered fixed, whereas the *kespen*-to-pile connection, which is a mortise and tenon joint, is represented using a spring with a rotational stiffness of 4E+08 N-mm/rad [60] ($k_{pile,}$ $_{kesp}$ in Fig. 10b) The Tier 2 model does not include soil explicitly. Consequently, to represent the soil's presence adjacent to the masonry wall ($k_{soil,wall}$ in Fig. 10b) and beneath the timber floor ($k_{soil,floor}$ in Fig. 10b), non-linear boundary interface elements, operative solely under compression, are employed. The soil's interaction with the piles is simulated through linear elastic boundary interface elements approximating the subgrade reaction (k_h and k_v in Fig. 10b), estimated using Vesić's [61] methodologies for timber piles. Moreover, the soil's contact at the timber pile tips is modelled with non-linear, no-tension boundary point elements (k_{tip} in Fig. 10b).

Material properties for masonry are sourced from NPR9998 [62], the seismic assessment guidelines developed in recent years in the Netherlands. This study specifically adopts properties for clay brick masonry constructed before 1945, as detailed in [62]. These values are based on experimental evaluations of material properties of existing Dutch unreinforced masonry buildings, thereby implicitly accounting for potential correlations between different material properties of the same material. However, it is important to note an ongoing experimental campaign that is focusing on the mechanical characterisation of masonry in Amsterdam's quays [63]. The tensile and shear strengths of the mortar joint at the wall-floor ($k_{wall,floor}$) junction are assumed to be equivalent to those of the masonry. Timber piles are classified as C24 grade according to [54], with their material properties obtained from Eurocode 5 [64]. The soil material properties used to calculate the stiffness of springs ($k_{soil,wall}$, $k_{soil,floor}$, k_h, k_v, and k_{tip}), simulating the soil's influence in Tier 2, are derived from Cone Penetration Tests (CPTs) performed at *Marnixkade* [54]. Table 1 compiles all material properties utilized in the Tier 2 model.

For all simulations, the Secant BFGS (Quasi-Newton) method is employed as the iterative method. The displacement norm must be satisfied during the iterative procedure with a tolerance of 1 %. The Parallel Direct Sparse method is utilised to solve the system of equations. The line search algorithm, which helps to overcome potential convergence problems in the highly non-linear range, is also adopted. Second-order effects are considered via the Total Lagrange geometrical nonlinearity. For the 3D dynamic moving load procedure, a Rayleigh damping ratio of 2 % is used in the calculations based on the

recommendations in NPR 9998 [62], which suggest values between 2 % and 8 % for masonry and 2 % for timber structures, albeit under seismic loading. Implicit time step integration using the Hilber Hughes-Taylor method [65], also known as the α method, is used to perform the dynamic analyses, adopting a value for α equal to − 0.1 and a time step of 0.001 s. In addition to traffic loads, static loads applied directly to the Tier 2 numerical model include the gravity load, which is automatically calculated by the software based on the density assigned to each material, and the dead load due to the weight of the capstone. Soil and water pressure are also applied horizontally to the wall. The vertical components of soil and water pressure are applied to the floor.

3.2.2. Load redistribution due to dynamic vs. static application of traffic loads

As discussed in Section 2.1, load redistribution due to dynamic vs. static application of traffic loads is quantified by comparing the structural capacity of the retaining structure as determined through the 3D dynamic and 3D static moving load procedures. Fig. 11 illustrates the evolution of out-of-plane (OOP) displacements of the retaining structure as the fire truck traverses it dynamically at three moments: (a) as the fire truck enters and reaches a quarter of the structure's length (*L/4*), (b) when positioned at the midpoint (*L/2*), and (c) as the fire truck approaches the three-quarters mark (*3 L/4*) towards exit. Limited deformations are observed, and the wall is observed to have sustained no damage based on the monitored strains, which do not exceed the threshold required for cracking. To evaluate the structure's load-bearing capacity, incremental analyses are performed, incrementing the fire truck's weight, effectively scaling up the stresses represented by σ_{Wall} and σ_{Floor} using monotonically increasing Load Multiplier (*LM*) values. OOP displacements and crack widths for different values of *LM* in these simulations are reported in Fig. 12 to Fig. 14.

In the performed incremental analyses, the retaining structure displays a seemingly linear elastic response up to *LM* value of 5 (Fig. 15a). Even at an *LM* of 10, the maximum out-of-plane (OOP) displacements are restricted to approximately 14 mm. Diagonal cracking is observed in the masonry wall as the truck traverses, albeit with limited crack width (Fig. 12). A particularly interesting observation is the ability of some of the cracks to close once the truck has moved beyond. This is observed by comparing the extent and width of cracks between Fig. 12b and Fig. 12c. This phenomenon can be attributed to load redistribution due to the consideration of dynamic loading conditions, which facilitates crack closure as the stress state transitions from tensile to compressive. At an *LM* of 20, as the truck enters the retaining structure, the wall experiences extensive cracking, with crack widths and OOP displacements significant enough to indicate a potential collapse. Contrary to the outcomes at *LM* = 10, the cracks formed remain open post-traversal, extending through the wall's entire thickness, and a pronounced flexural crack near the base suggests the wall's imminent overturning (Fig. 13) For higher load multipliers, such as at *LM* = 22, the wall exhibits similarly

Table 1
Summary of material properties adopted in the Tier 2 numerical model.

		Masonry	Timber	Interface Stiffness			
Property	Unit	Value	Value	Property	Direction	Unit	Value
Young's modulus	MPa	5000	11000	$k_{soil,wall}$	Normal	N/mm^3	0.027
Poisson's ratio	-	0.25	0.35		Tangential	N/mm^3	0.022
Density	Kg/m^3	1950	420	$k_{soil,floor}$	Normal	N/mm^3	0.027
Tensile strength	MPa	0.1			Tangential	N/mm^3	0.022
Fracture energy in tension	N/mm	0.01		k_h*	Horizontal**	N/mm^3	0.004 to 0.008
Compressive strength	MPa	8.5		k_v*	Vertical**	N/mm^3	1.678E-08 to 3.36E-07
Fracture energy in compression	N/mm	20		k_{tip}	Normal	N/mm^3	0.415
				$k_{wall,floor}$	Normal	N/mm^3	39.957
					Tangential	N/mm^3	105.344
				$k_{pile,kesp}$	Rotational	N-mm/rad	4×10^8

* Varies along the depth of the pile, range of values is provided
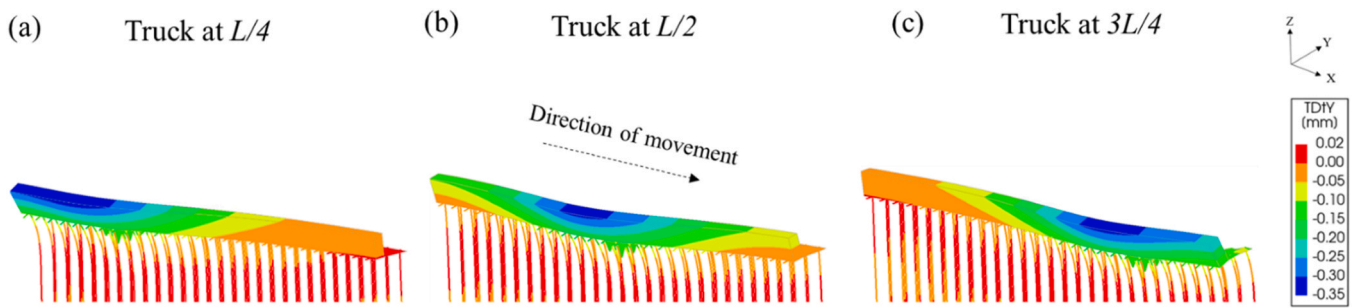** Refers to the direction of component of subgrade reaction

Fig. 11. Out-of-plane displacements of the retaining structure during the passage of the fire-truck (*LM* = 1) at different instants: truck at (a) *L/4*; (b) *L/2* and (c) *3 L/4*. adopting the 3D dynamic moving load procedure (Deformation scale factor = 5000).
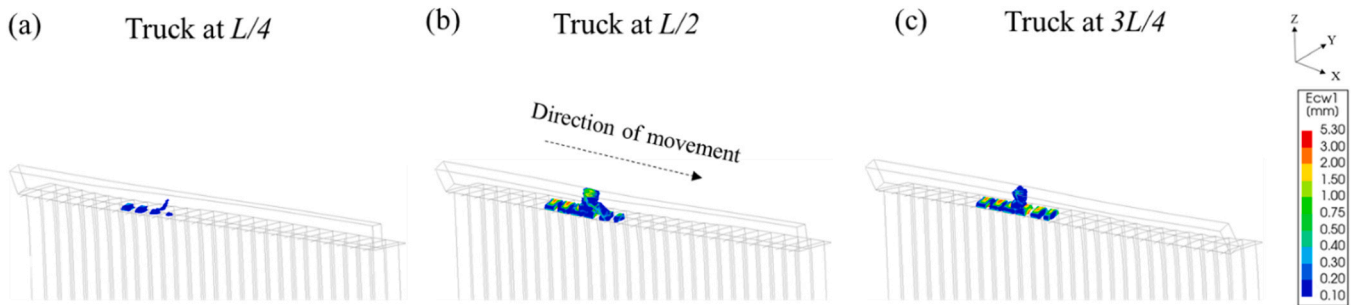

Fig. 12. Principal crack widths of the retaining structure during the passage of the fire-truck (*LM* = 10) at different instants: truck at (a) *L/4*; (b) *L/2* and (c) *3 L/4*. adopting the 3D dynamic moving load procedure (Deformation scale factor = 100).
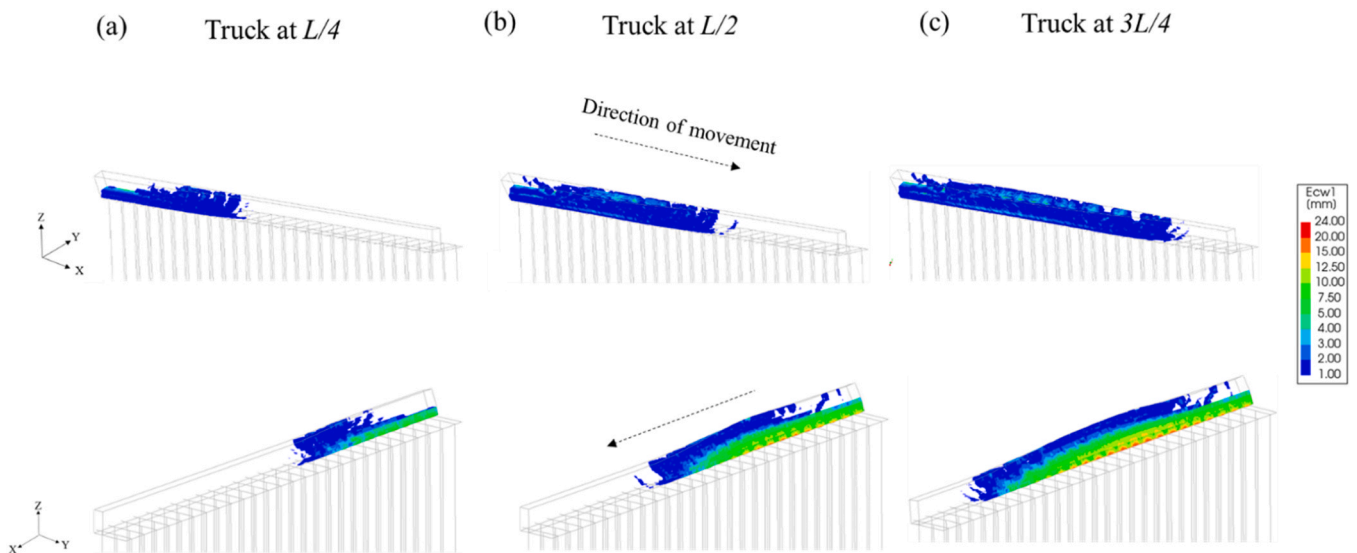

Fig. 13. Principal crack widths of the retaining structure during the passage of the fire-truck (*LM* = 20) at different instants: truck at (a) *L/4*; (b) *L/2* and (c) *3 L/4*. adopting the 3D dynamic moving load procedure (Deformation scale factor = 10).

extensive cracking as observed at *LM* = 20, albeit with increased crack widths and OOP displacements. Additionally, at these higher *LM* values, a significant portion of the timber sub-structure begins to display stress levels surpassing their predefined strength limits [64].

The described load redistribution is not observed in the incremental analyses performed with the 3D static moving load procedure. The retaining structure exhibits seemingly linear elastic behaviour until a *LM* value of 24. However, at *LM* = 26, a sudden shift is noted, with the retaining structure displaying behaviours indicative of imminent collapse. As the fire truck exits the retaining structure, local overturning of a segment of the wall is evidenced by significant OOP displacements

and crack widths (Fig. 14a). Increasing the *LM* value to 28 results in failure occurring at the truck's entrance to the vicinity of the structure (Fig. 14b). However, the peak reaction force sustained by the wall remains consistent with that observed at *LM* = 26 indicating that the failure mechanism is force-controlled (Fig. 15a).

The enhanced structural capacity of the retaining structure is due to load redistribution under dynamic loading conditions. This is demonstrated by its ability to withstand higher reaction forces with hardening behaviour for increasing values of *LM*, as clearly illustrated by the curves depicting wall reaction force vs. displacement. These curves, presented in Fig. 15a, are derived from both the static and dynamic moving load
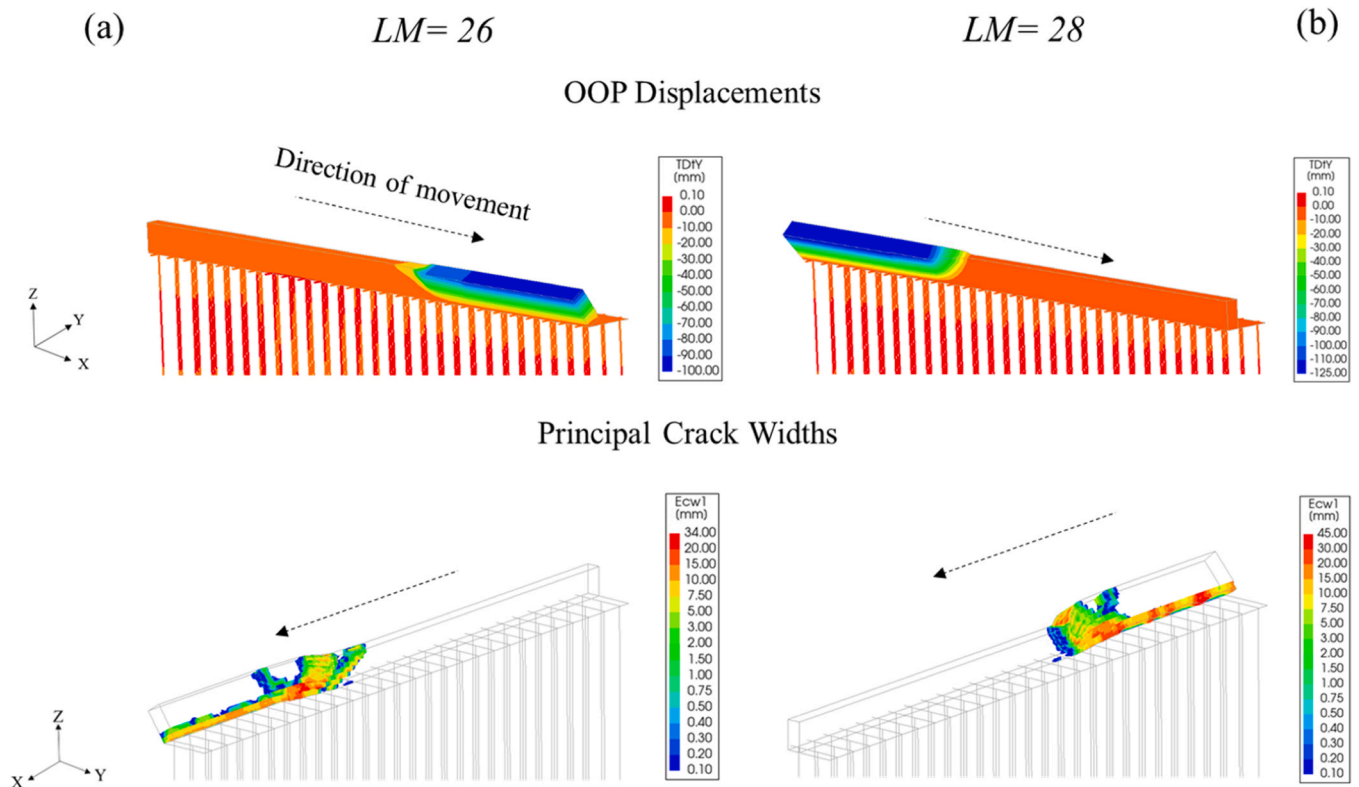
Fig. 14. Failure mechanism in terms of out-of-plane displacements and principal crack widths of the retaining structure during the passage of the fire-truck (a) *LM = 26* and (b) *LM = 28* adopting the 3D static moving load procedure (Deformation scale factor = 10).
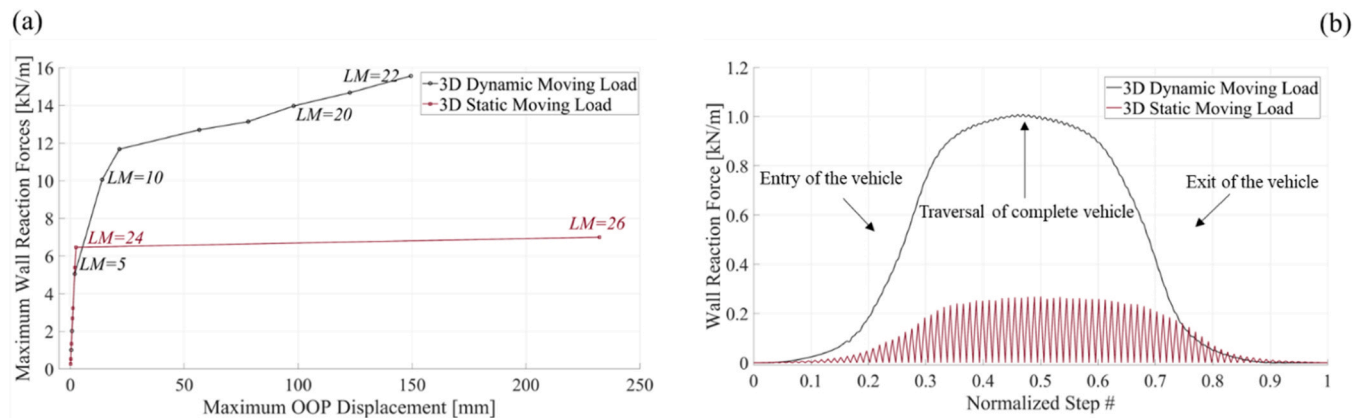

Fig. 15. Comparison between 3D dynamic and static moving load procedures of (a) maximum wall reaction force vs. maximum out-of-plane displacement curves and (b) reaction forces developed in the wall when a fire-truck (*LM = 1*) traverses along the retaining structure plotted against step #.

simulations, highlighting the significant impact of accounting for dynamic loading. In these graphs, the peak reaction forces noted in the masonry wall for a specific *LM* value are plotted against the maximal OOP displacement recorded in the corresponding analysis. Additionally, the peak reaction force is normalised with respect to the length of the retaining structure, $L = 30$ m. It also becomes evident from Fig. 15a that the retaining structure encounters significantly higher forces when subjected to the same traffic load, i.e. the same value of *LM*, if this load is applied dynamically rather than statically. This is because the 3D static moving load assessment procedure simulates the truck's transit along the retaining structure assuming an infinitely slow velocity. As a result, the time Δt needed for the truck to traverse the segmental distance Δd is infinitely prolonged. Consequently, the structure is exposed to only a single σ_{Wall} stress distribution at any given step as the vehicle moves

across it. In contrast, the 3D dynamic moving load procedure entails multiple σ_{Wall} distributions acting concurrently, with the number of simultaneous distributions reliant on Δt and also the time span during which σ_{Max} reduces to zero. This is evident from Fig. 15b which depicts the reaction forces generated in the wall (again normalised with respect to the length of the retaining structure) as the fire truck (*LM = 1*) traverses along it, when the retaining structure behaves elastically in both assessment procedures. The observed plateau in reaction forces across both procedures in Fig. 15b corresponds to the phase where the entire truck traverses along the structure. The periods of increasing or decreasing forces indicate the vehicle's entry into or exit from the immediate vicinity of the modelled segment of the retaining structure.

3.2.3. Load redistribution due to 3D vs. 2D numerical modelling

As discussed in Section 2.2, the spatial load redistribution related to the three-dimensional modelling of the earth retaining structure is quantified by comparing the structural capacity as determined through both the 3D and 2D monotonic load procedures. The force-displacement capacity curve obtained from the 3D monotonic load procedure is illustrated in Fig. 16. The forces represent the total reaction that the wall sustains normalized by the length of the wall, while the displacements are the maximum out-of-plane displacement measured across the wall at each load step. To monitor the load redistribution mechanisms attributable to the 3D configuration of the retaining structure, the reaction forces sustained by consecutive, individual 1.1 m sections of the wall are tracked in Fig. 17 and Fig. 18. This allows for a comprehensive analysis of the evolution of the reaction forces along the length of the wall, particularly in relation to the occurrence of cracking within the masonry, when the *LM* values (and, consequently, the σ_{Wall} and σ_{Floor} stresses) are progressively increased. The total wall reaction force plotted in Fig. 16 can also be derived by simply summing up the contributions from all the individual 1.1 m sections and then dividing it by the wall length. The σ_{Wall} stress distribution calculated in Tier 1 using the analytical formulation (i.e. Fig. 9c), as detailed in Section 2.3, is also utilised to conduct a comparison of the outcomes of the 3D monotonic load procedure when numerical- and analytical-based stress distributions are considered. The normalized wall reaction force vs. displacement curve is illustrated for both the cases in Fig. 16. Despite the relative simplicity and lower computational cost of determining σ_{Wall} through the analytical formulation compared to its numerical evaluation, the structural capacity and the force-displacement curve as well as the failure mechanism, derived from both analytical and numerical assessments of σ_{Wall}, demonstrate noteworthy concordance.

As evident from the force-displacement curves presented in Fig. 16, the wall demonstrates elastic behaviour up to a *LM* value of 52.4. Consistently, no cracking occurs up to this same *LM*, as illustrated in Fig. 17b. Furthermore, the reaction forces sustained by the individual 1.1 m sections of the wall mirror the shape of the σ_{Wall} profile, maintaining a linear relationship with *LM* for values up to and including 52.4. While sub-horizontal cracking is also observed towards the base of the central portion of the wall, these cracks do not penetrate the entire thickness of the wall and exhibit limited widths on the water-facing side of the retaining structure. For increasing loads, while the total reaction force sustained by the wall continues to increase, such increment is accompanied by a reduction in stiffness due the described cracking (Fig. 16). At an *LM* value of 52.6, it is observed that the reaction forces

sustained by the 1.1 m sections where large cracks are recorded diminish. Additionally, the distribution of reaction forces along the wall's span also ceases to mirror the profile of σ_{Wall}, with the reaction forces from the cracked regions being redistributed mostly towards the wall's centre.

At *LM* = 52.8, as cracking in the wall becomes increasingly severe – including the central portion, though relatively less so compared to the regions flanking it (Fig. 18b) – the total reaction force that can be sustained by the wall starts decreasing (Fig. 16). The central 1.1 m section still sustains a greater reaction force than its adjoining sections (Fig. 18b), but this could also be simply attributed to the shape of σ_{Wall}, which subjects the central portion of the wall to the highest compressive force. At *LM* = 53.0, the cracking at the base of the central section of the wall becomes too severe for this section to sustain more reaction forces, and the load from this section is redistributed to its adjoining sections (Fig. 18a).

The selection of 1.1 m segments for tracking load redistribution along the wall in the 3D monotonic load procedure mirrors the spacing between piles within the retaining structure, which also corresponds to the thickness designated for the Tier 2 numerical model in the 2D monotonic load procedure. As depicted in Fig. 9b, the σ_{Wall} compressive stresses at the base of the wall are concentrated in the central section, extending approximately 11 m from 9 to 20 m (ΔL), and tapers off to negligible levels beyond this range. This observation leads to the selection of ten segments 1.1 m wide within this central 11 m zone, which are utilized in 2D monotonic analyses to determine the lower and upper bounds of structural capacity. The 2D monotonic load procedure as outlined in Section 2.2.2/Fig. 5b is adopted for each 2D model by considering the σ_{Wall} distribution corresponding to the location of the segment. It is worth noticing that 10 composed elements are included in the 3D model in the locations corresponding to each section, allowing for a direct comparison of the curves plotting the reaction forces transferred at the base of each section of the wall and the maximum recorded out-of-plane displacements.

No cracking is observed in the wall in any of the 2D monotonic analyses, with the wall tilting around its base due to the opening of the wall-floor interface, as depicted in Fig. 19a. This phenomenon underscores the absence of load redistribution in the 2D monotonic analyses and significantly impacts the evaluated force capacities of the retaining structure, resulting in all capacity curves obtained from the 2D procedure demonstrating lower structural capacity compared to those from the 3D procedure. The comparison is illustrated in Fig. 19b, where force-displacement capacity curves from the 2D monotonic analyses
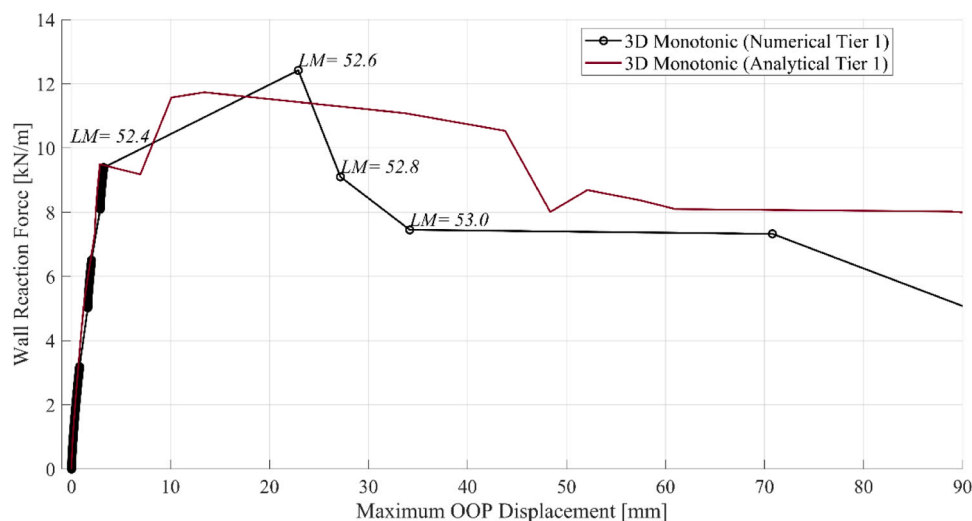

Fig. 16. Comparison of wall reaction force vs. maximum out-of-plane displacement curves from 3D monotonic load procedure adopting numerical and analytical evaluations of σ_{Wall} in Tier 1.
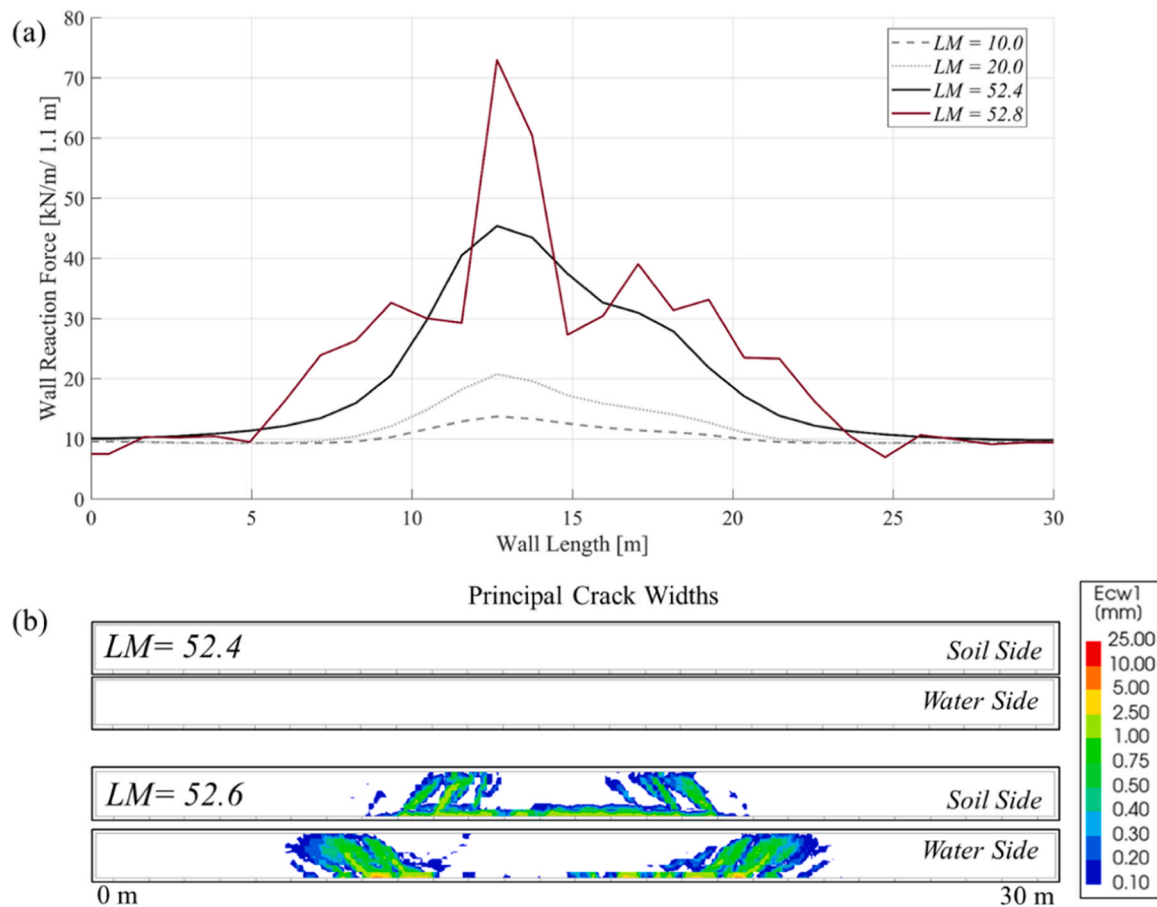
Fig. 17. Distribution of (a) wall reaction forces and (b) principal crack widths along the length of the wall in the 3D monotonic load procedure at *LM* = 52.4 and *LM* = 52.6.

(*2D-1* to *2D-10*) are compared with those derived from the 3D monotonic analyses (*3D-1* to *3D-10*). The 3D monotonic analyses result in force-capacities 1.16 to 2.90 times higher than their 2D counterparts. Importantly, the curves from the 3D procedure, corresponding to the reaction forces and displacements developed in the individual 1.1 m sections, do not require normalization relative to the model's length for comparative analysis. This methodology ensures a comparison between the load distributions on the 3D and 2D models as closely matched as possible. Nonetheless, they are not identical, because the σ_{Wall} vs. height distributions in the 2D models remain constant across the model's thickness, unlike the slight variations observed across 1.1 m in the 3D models.

4. Concluding remarks

This paper introduces analysis procedures for assessing existing masonry earth retaining structures under traffic loading. These procedures account for load redistribution mechanisms within masonry, which are currently neglected in the conventional methods, thereby allowing for less conservative predictions of the structural capacity. Redistribution mechanisms arising from both time and spatial variations of traffic loads in 3D configurations of masonry earth retaining structures are considered, resulting in four analysis procedures: (i) 3D dynamic moving load, (ii) 3D static moving load, (iii) 3D monotonic, and (iv) 2D monotonic.

By comparing the structural capacities evaluated via the application of the four assessment procedures, it is possible to quantify the load redistribution within the structure arising solely from the consideration of either dynamic versus static loading, or 3D versus 2D structural

configurations of retaining structures. Such a possibility is demonstrated through the application of the developed analysis procedures to the assessment of an existing masonry retaining structure in Amsterdam, the Netherlands, for which the increase in structural capacity resulting from load redistribution is quantified. For this specific case study, the retaining structure is subjected to approximately 3.7 times higher forces when the same traffic load is applied dynamically rather than statically. This increment is caused in the 3D dynamic moving load procedure by the superposition of loads, determined by the movement of a vehicle along the earth retaining structure, which is neglected in the static application of the loading. Nevertheless, the dynamic application of the vehicular loading results in the retaining structure exhibiting a 110 % larger force capacity, as well as a significantly more ductile behaviour. Additionally, also considering the 3D configuration of the retaining structure leads to an increase of the predicted lateral force capacity. Specifically, values 1.16 to 2.90 times higher than those calculated assuming a 2D configuration are obtained. This increased capacity arises from the structure's ability to redistribute loads along its length after cracking, which cannot be captured in 2D analysis procedures.

Future work should concentrate on the validation of the developed analysis procedures against experimental investigations. The implications of the sub-structure approach adopted in all the analysis procedures developed in this paper, i.e. they treat the backfill, over which vehicular traffic moves, and the retaining structure itself as separate entities should also be evaluated. Such investigations should also include understanding the impact of modelling energy dissipation and radiation damping of the backfill on the structural demand that the retaining structure is subjected to. Additionally, for the moving load procedures, investigating the effects of considering multiple vehicle
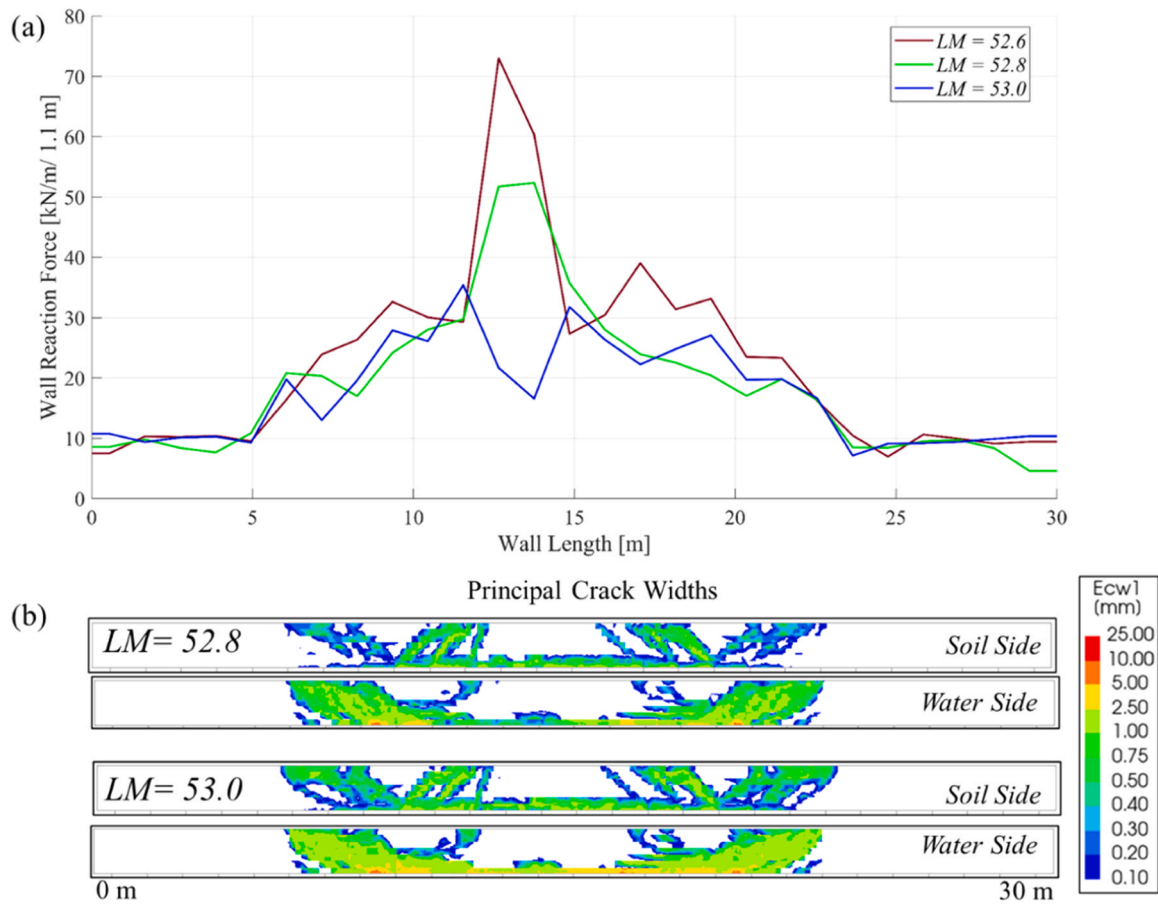
Fig. 18. Distribution of (a) wall reaction forces and (b) principal crack widths along the length of the wall in the 3D monotonic load procedure at *LM* = 52.8 and *LM* = 53.0.
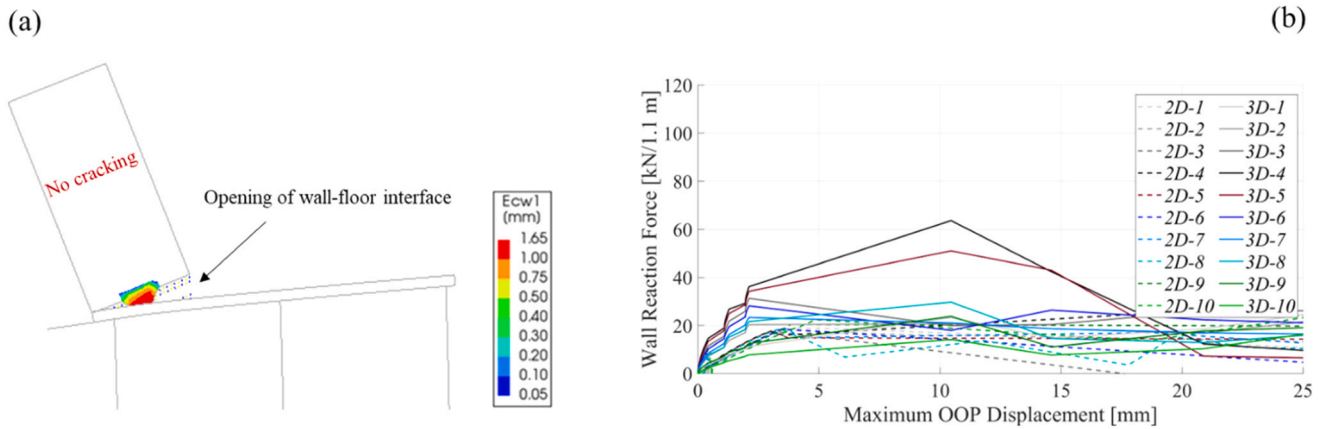

Fig. 19. (a) Failure mechanism in all 2D monotonic analyses and (b) comparison of wall reaction force vs. maximum out-of-plane displacement curves from 2D and 3D monotonic load procedures.

passages and the resultant damage accumulation, as opposed to simply increasing the traffic load associated with a single vehicle to assess structural capacity, warrants further examination.

CRediT authorship contribution statement

Satyadhrik Sharma: Writing – original draft, Visualization, Validation, Methodology, Formal analysis, Data curation, Conceptualization. **Michele Longo:** Writing – review & editing, Visualization, Software, Methodology, Investigation, Formal analysis, Data curation,

Conceptualization. **Francesco Messali:** Writing – review & editing, Supervision, Project administration, Methodology, Funding acquisition, Conceptualization.

Declaration of Competing Interest

The authors declare that they have no known competing financial interests or personal relationships that could have appeared to influence the work reported in this paper.

Data availability

Data will be made available on request.

References

[1] Gemeente Amsterdam. Actieplan Bruggen en Kademuren 2023–2026. Amsterdam, the Netherlands: 2022.

[2] Sharma S, Longo M, Messali F. A novel tier-based numerical analysis procedure for the structural assessment of masonry quay walls under traffic loads. Front Built Environ 2023;9. https://doi.org/10.3389/fbuil.2023.1194658.

[3] O REILLY MP, BUSH DI, BRADY KC, POWRIE W. The stability of drystone retaining walls on highways. Proc Inst Civ Eng - Munic Eng 1999;133:101–7. https://doi.org/10.1680/imuen.1999.31763.

[4] McCombie PF, Mundell C, Heath A, Walker P. Drystone retaining walls: ductile engineering structures with tensile strength. Eng Struct 2012;45:238–43. https://doi.org/10.1016/j.engstruct.2012.06.046.

[5] Hough A. Assessment of historical railway retaining walls. Proc Inst Civ Eng - Transp 2001;147:217–21. https://doi.org/10.1680/tran.2001.147.4.217.

[6] Odent N. Recensement des ouvrages de soutènement en bordure du réseau routier national. Ouvrage d'Art 2000;34:15–8.

[7] DeMarco M.J., Barrows R.J., Lewis S. NPS Retaining Wall Inventory and Assessment Program (WIP): 3,500 Walls Later. Earth Retention Conference 3, Reston, VA: American Society of Civil Engineers; 2010, p. 870–7. https://doi.org/10.1061/41128(384)87.

[8] Arya AS, Gupta VP. Retaining wall for hill roads. Indian Road Congr J 1983;44: 291–326.

[9] Gupta VP, Lohani NK. Treatment and repair of partially damaged retaining walls in hills. Indian Highw 1982;10:20–8.

[10] Venmans AAM, op de Kelder M, de Jong J, Korff M, Houtepen M. Reliability of InSAR satellite monitoring of buildings near inner city quay walls. Proc Int Assoc Hydrol Sci 2020;382:195–9. https://doi.org/10.5194/piahs-382-195-2020.

[11] Hain A, Zaghi AE. Applicability of photogrammetry for inspection and monitoring of dry-stone masonry retaining walls. Transp Res Rec: J Transp Res Board 2020; 2674:287–97. https://doi.org/10.1177/0361198120929184.

[12] European Investment Bank. The state of local infrastructure investment in Europe EIB municipalities survey 2022–2023. Kirchberg, Luxembourg: 2023.

[13] Lourenço PB. Computations on historic masonry structures. Prog Struct Eng Mater 2002;4:301–19. https://doi.org/10.1002/pse.120.

[14] Franza A, DeJong MJ. Elastoplastic Solutions to Predict Tunneling-Induced Load Redistribution and Deformation of Surface Structures. J Geotech Geoenviron Eng 2019;145. https://doi.org/10.1061/(ASCE)GT.1943-5606.0002021.

[15] Lourenco PB, Silva LC. Computational applications in masonry structures: from the meso-scale to the super-large/super-complex. Int J Multiscale Comput Eng 2020; 18:1–30. https://doi.org/10.1615/IntJMultCompEng.2020030889.

[16] AASHTO. AASHTO LRFD BRIDGE DESIGN SPECIFICATIONS. 2010.

[17] CEN. EN 1991–2 (2003): Eurocode 1: Actions on structures - Part 2: Traffic loads on bridges. 2003.

[18] CSA. CAN/CSA-S6–06 Canadian Highway Bridge Design Code. 2019.

[19] CIRIA. Report C580 Embedded retaining walls – guidance for economic design. 2017.

[20] DeJong M.J. Seismic assessment strategies for masonry structures. PhD Thesis. Massachusetts Institute of Technology, 2009.

[21] Lourenço PB, Mendes N, Marques RFP. Earthquake design and assessment of masonry structures: review and applications. Trends in Civil and Structural Engineering Computing. Stirlingshire, Scotland, United Kingdom: Saxe-Coburg Publications; 2009. p. 77–101.

[22] Parisse F, Cattari S, Marques R, Lourenço PB, Magenes G, Beyer K, et al. Benchmarking the seismic assessment of unreinforced masonry buildings from a blind prediction test. Structures 2021;31:982–1005. https://doi.org/10.1016/j.istruc.2021.01.096.

[23] Milani G, Lourenco PB. Blast analysis of enclosure masonry walls using homogenization approaches. Int J Multiscale Comput Eng 2009;7:91–113. https://doi.org/10.1615/IntJMultCompEng.v7.i2.30.

[24] Godio M, Williams Portal N, Flansbjer M, Magnusson J, Byggnevi M. Experimental and numerical approaches to investigate the out-of-plane response of unreinforced masonry walls subjected to free far-field blasts. Eng Struct 2021;239:112328. https://doi.org/10.1016/j.engstruct.2021.112328.

[25] Anas S.M., Alam M., Umair M. Out-of-plane Response of Clay Brick Unreinforced and Strengthened Masonry Walls Under Explosive-induced Air-blast Loading, 2022, p. 477–491. https://doi.org/10.1007/978–981-16–6978-1_37.

[26] Silva LC, Lourenço PB, Milani G. Rigid block and spring homogenized model (HRBSM) for masonry subjected to impact and blast loading. Int J Impact Eng 2017;109:14–28. https://doi.org/10.1016/j.ijimpeng.2017.05.012.

[27] Pelà L, Aprile A, Benedetti A. Seismic assessment of masonry arch bridges. Eng Struct 2009;31:1777–88. https://doi.org/10.1016/j.engstruct.2009.02.012.

[28] Pelà L, Aprile A, Benedetti A. Comparison of seismic assessment procedures for masonry arch bridges. Constr Build Mater 2013;38:381–94. https://doi.org/10.1016/j.conbuildmat.2012.08.046.

[29] Addessi D, Gatta C, Nocera M, Liberatore D. Nonlinear dynamic analysis of a masonry arch bridge accounting for damage evolution. Geosci (Basel) 2021;11: 343. https://doi.org/10.3390/geosciences11080343.

[30] Rota M, Pecker A, Bolognini D, Pinho R. A methodology for seismic vulnerability of masonry arch bridge walls. J Earthq Eng 2005;9:331–53. https://doi.org/10.1142/S1363246905002432.

[31] Forgács T, Sarhosis V, Ádány S. Shakedown and dynamic behaviour of masonry arch railway bridges. Eng Struct 2021;228:111474. https://doi.org/10.1016/j.engstruct.2020.111474.

[32] Sobczyk B, Pyrzowski Ł, Miśkiewicz M. Computational modelling of historic masonry railroad arch bridges. Comput Struct 2024;291:107214. https://doi.org/10.1016/j.compstruc.2023.107214.

[33] Grosman S, Macorini L, Izzuddin BA. Parametric nonlinear modelling of 3D masonry arch bridges. Adv Eng Softw 2023;185:103514. https://doi.org/10.1016/j.advengsoft.2023.103514.

[34] Sarhosis V, De Santis S, de Felice G. A review of experimental investigations and assessment methods for masonry arch bridges. Struct Infrastruct Eng 2016;12: 1439–64. https://doi.org/10.1080/15732479.2015.1136655.

[35] Kuai H., Macchiarulo V., Sharma S., Karamitopoulos P., Messali F., Giardina G. MT-InSAR Optimisation for Structural Health Monitoring. European Workshop on Structural Health Monitoring (EWSHM), Potsdam, Germany: 2024.

[36] Gemeente Amsterdam. Voortgangrapportage – Programma Bruggen en Kademuren. Https://OpenresearchAmsterdam/Image/2022/10/6/Vgr_en_themabijlage_bruggen_kademuren_september_2022Pdf (in Dutch) 2022.

[37] Vytiniotis A, Panagiotidou A-I, Whittle AJ. Analysis of seismic damage mitigation for a pile-supported wharf structure. Soil Dyn Earthq Eng 2019;119:21–35. https://doi.org/10.1016/j.soildyn.2018.12.020.

[38] Longo M, Sousamli M, Korswagen PA, van Staalduinen P, Rots JG. Sub-structure-based 'three-tiered' finite element approach to soil-masonry-wall interaction for light seismic motion. Eng Struct 2021;245:112847. https://doi.org/10.1016/j.engstruct.2021.112847.

[39] Song C, Wolf JP. The scaled boundary finite-element method—alias consistent infinitesimal finite-element cell method—for elastodynamics. Comput Methods Appl Mech Eng 1997;147:329–55. https://doi.org/10.1016/S0045-7825(97)00021-2.

[40] Wegner JL, Yao MM, Zhang X. Dynamic wave–soil–structure interaction analysis in the time domain. Comput Struct 2005;83:2206–14. https://doi.org/10.1016/j.compstruc.2005.04.004.

[41] Zhang X, Wegner JL, Haddow JB. Three-dimensional dynamic soil-structure interaction analysis in the time domain. Earthq Eng Struct Dyn 1999;28:1501–24. https://doi.org/10.1002/(SICI)1096-9845(199912)28:12<1501::AID-EQE878>3.0.CO;2-8.

[42] Karabalis DL, Mohammadi M. 3-D dynamic foundation-soil-foundation interaction on layered soil. Soil Dyn Earthq Eng 1998;17:139–52. https://doi.org/10.1016/S0267-7261(97)00047-X.

[43] Halabian AM, El Naggar MH. Effect of non-linear soil–structure interaction on seismic response of tall slender structures. Soil Dyn Earthq Eng 2002;22:639–58. https://doi.org/10.1016/S0267-7261(02)00061-1.

[44] Abdel-Karim AM, Tadros MK, Benak j:V. Live load distribution on concrete box culverts. Transp Res Rec 1990;1288:136–51.

[45] Lysmer J, Kuhlemeyer RL. Finite Dynamic Model for Infinite Media. J Eng Mech Div 1969;95:859–77. https://doi.org/10.1061/JMCEA3.0001144.

[46] Vamvatsikos D, Cornell CA. Incremental dynamic analysis. Earthq Eng Struct Dyn 2002;31:491–514. https://doi.org/10.1002/eqe.141.

[47] Spangler MG, Mickle JL. Lateral pressures on retaining walls due to backfill surface loads. Pressure-deformation measurements in earth. Highway Research Board,; 1956.

[48] James RW, Brown DE. Wheel-Load-Induced Earth Pressures on Box Culverts. Transp Res Rec 1987;1129:55–62.

[49] Frazee GR. New Formulations of Boussinesq Solution for Vertical and Lateral Stresses in Soil. Pract Period Struct Des Constr 2021;26. https://doi.org/10.1061/(ASCE)SC.1943-5576.0000567.

[50] Boussinesq J. Application des potentiels à l'étude de l'équilibre et du mouvement des solides élastiques. Proceedings of Mémoires de la Société des Sciences, 4e Série, Tome XIII. Paris: Gauthier-Villars; 1885. p. 104–7.

[51] Rijkswaterstaat. https://www.rijkswaterstaat.nl/en/water/water-management 2023.

[52] Gemeente Amsterdam. https://www.amsterdam.nl/projecten/kademuren/ 2023.

[53] Korff M, Hemel M-J, Peters DJ. Collapse of the Grimburgwal, a historic quay in Amsterdam, the Netherlands. Proc Inst Civ Eng - Forensic Eng 2022;175:96–105. https://doi.org/10.1680/jfoen.21.00018.

[54] NEBEST B.V. Marnixkade in Amsterdam. Funderingsonderzoek. Ref: 27854–01-01, definitive. Vianen, the Netherlands: 2016.

[55] Rijkswaterstaat. https://www.rijkswaterstaat.nl/zakelijk/open-data/normaal-amsterdams-peil 2023.

[56] Loulizi A, Al-Qadi IL, Lahouar S, Freeman TE. Measurement of Vertical Compressive Stress Pulse in Flexible Pavements: Representation for Dynamic

Loading Tests. Transp Res Rec: J Transp Res Board 2002;1816:125–36. https://doi.org/10.3141/1816-14.

[57] DIANA F.E.A. User's Manual - Release 10.7. Delft, the Netherlands: 2023.

[58] Schreppers; G.M.A., Garofano A., Messali F., Rots J.G. DIANA Validation report for Masonry modelling. Delft, the Netherlands: 2016.

[59] Lourenço P. Computational strategies for masonry structures. PhD Thesis. Technische Universiteit Delft, 1996.

[60] Ingenieursbureau Gemeente Amsterdam. Toetskader Amsterdamse Kademuren (TAK 3.2). Amsterdam, the Netherlands: 2023.

[61] Vesić AB. Bending of Beams Resting on Isotropic Elastic Solid. J Eng Mech Div 1961;87:35–53. https://doi.org/10.1061/JMCEA3.0000212.

[62] NEN. Assessment of structural safety of buildings in case of erection, reconstruction and disapproval – Induced earthquakes – Basis of design, actions and resistances. NPR9998+C1:2020. 2020.

[63] Li X, Esposito R. A strategy for material characterisation of multi-wythe masonry Infrastructure: Preliminary study. Constr Build Mater 2023;408:133600. https://doi.org/10.1016/j.conbuildmat.2023.133600.

[64] CEN. EN 1995–1 (2004): Eurocode 5: Design of timber structures - Part 1–1: General - Common rules and rules for buildings. 2004.

[65] Hilber HM, Hughes TJR, Taylor RL. Improved numerical dissipation for time integration algorithms in structural dynamics. Earthq Eng Struct Dyn 1977;5:283–92. https://doi.org/10.1002/eqe.4290050306.